



Full Text View

[Volume 32, Issue 9 \(September 2002\)](#)
Journal of Physical Oceanography

 Article: pp. 2681–2705 | [Abstract](#) | [PDF \(2.46M\)](#)

A Non-normal View of the Wind-Driven Ocean Circulation

Andrew M. Moore, Cristina L. Perez, and Javier Zavala-Garay
Program in Atmospheric and Oceanic Sciences, and Cooperative Institute for Research in Environmental Sciences, University of Colorado, Boulder, Colorado

(Manuscript received April 16, 2001, in final form March 4, 2002)

DOI: 10.1175/1520-0485(2002)032<2681:ANNVOT>2.0.CO;2

ABSTRACT

Generalized linear stability theory is applied to the wind-driven ocean circulation in the form of a double gyre described by the barotropic quasigeostrophic vorticity equation. The development of perturbations on this circulation is considered. The circulation fields are inhomogeneous, and regions of straining flow render non-normal the tangent linear operators that describe the time evolution of perturbation energy and enstrophy. When the double-gyre circulation is asymptotically stable, growth of perturbation energy and enstrophy is still possible due to linear interference of its nonorthogonal eigenmodes. The sources and sinks of perturbation energy and enstrophy associated with the interference process are traditionally associated with the interaction of perturbation stresses with the mean flow. These ideas are used to understand the response of an asymptotically stable double-gyre circulation to stochastic wind stress forcing. Calculation of the optimal forcing patterns (stochastic optimals) reveals that much of the stochastically induced variability can be explained by one pattern. Variability induced by this pattern is maintained by long and short Rossby waves that interact with the western boundary currents, and perturbation growth occurs through barotropic processes. The perturbations that maintain the stochastically induced variance in this way have a large projection on some of the most non-normal, least-damped eigenmodes of the double-gyre circulation.

Perturbation growth in nonautonomous and asymptotically unstable systems is also considered in the same framework. The Lyapunov vectors of unstable flows are found to have a large projection on some of the most non-normal, least-damped eigenmodes of the time mean circulation.

Table of Contents:

- [Introduction](#)
- [The barotropic vorticity](#)
- [A double gyre basic-state](#)
- [Stochastically induced](#)
- [Nonautonomous systems](#)
- [Summary and discussion](#)
- [REFERENCES](#)
- [APPENDIX](#)
- [TABLES](#)
- [FIGURES](#)

Options:

- [Create Reference](#)
- [Email this Article](#)
- [Add to MyArchive](#)
- [Search AMS Glossary](#)

Search CrossRef for:

- [Articles Citing This Article](#)

Search Google Scholar for:

- [Andrew M. Moore](#)
- [Cristina L. Perez](#)
- [Javier Zavala-Garay](#)


1. Introduction

The stability of dynamical systems such as the atmosphere and oceans has been a subject of intense research for many years. The development of infinitesimal or finite amplitude perturbations on a preexisting flow field has obvious applications to a number of frequently encountered problems including turbulence, meander and eddy development, cyclogenesis, error growth in forecast models, and predictability. For many years the traditional approach to stability analysis of geophysical flows has been to examine the eigenmodes of the governing dynamical operators linearized about a preexisting circulation of interest under the basic assumption that, at least during the early stages of development, perturbations are described by linear dynamics. Thus, if at least one exponentially growing eigenmode exists, the system is deemed unstable. However, since the

pioneering work of [Rayleigh \(1880\)](#) and [Kelvin \(1887\)](#) it has been known that there are certain flows that do not possess any growing eigenmodes and yet are unstable in the laboratory.

A single eigenmode may describe the asymptotic growth or decay of a perturbation, but for a finite time interval, transient perturbation growth can result from the linear interference of several eigenmodes even if all of these modes are asymptotically stable. Therefore exponential instability is not an essential requirement for a system to support growing perturbations. From a mathematical viewpoint, a dynamical operator or matrix possesses nonorthogonal eigenmodes if it is non-normal. A non-normal system can support growing perturbations even if all of the eigenmodes of the associated linear operator are stable. This is merely a consequence of linear interference of the nonorthogonal eigenmodes that are linearly dependent on each other. The non-normality of a linear operator that describes perturbation development is associated with properties of the circulation that destroy the commutative properties of the operator with its adjoint. In the atmosphere and ocean this is often associated with shearing and straining flows. By considering the non-normality of a dynamical system it is possible to adopt a geometrical view of fluid instabilities, which can sometimes be more enlightening than the more classical approach to the problem.

The idea of the atmosphere as a non-normal system, and the ramifications of this for instability, has received considerable attention over the last two decades due primarily to the work of Farrell and coworkers ([Farrell 1982a,b, 1984, 1985, 1988a,b, 1989a,b, 1990; Farrell and Ioannou 1993a,b,c,d,e,f, 1994a,b, 1996a,b,c, 1999; Butler and Farrell 1992; DelSole and Farrell 1994, 1995; Ioannou 1995](#)). Other notable studies include [Zeng \(1983\)](#), [Boyd \(1983\)](#), [Branstator \(1985\)](#), [Zhang \(1988\)](#), [Mak and Cai \(1989\)](#), and [Borges and Hartmann \(1992\)](#). In fact, these ideas have been applied successfully to understand and explore various aspects of the atmospheric circulation including middle-latitude cyclogenesis ([Farrell 1982a,b, 1984, 1985, 1988a, 1989a](#)), frontal waves ([Joly 1995](#)), atmospheric blocking ([Zou et al. 1993](#)), the atmospheric energy spectrum ([Farrell and Ioannou 1993d](#)), quasigeostrophic turbulence ([DelSole 1996, 1999](#)), forecast error growth in atmospheric models ([Farrell 1990; Mureau et al. 1993; Molteni et al. 1993](#)), atmospheric predictability and ensemble weather prediction ([Lorenz 1965; Lacarra and Talagrand 1988; Ferranti et al. 1988; Farrell 1990; Errico et al. 1993; Buizza et al. 1993; Buizza and Palmer 1995; Palmer 1996; Buizza 1995, 1997; Molteni et al. 1996; Hartmann et al. 1995; Ehrendorfer and Tribbia 1997](#)), climate variability ([DelSole and Hou 1999](#)), and tropical air–sea interaction and El Niño ([Blumenthal 1991; Xue et al. 1994, 1997a,b, 1999; Moore and Kleeman 1996, 1997a,b, 1998, 1999a,b, 2001; Kleeman and Moore 1997, 1999; Penland 1989, 1996; Penland and Sardeshmukh 1995a,b; Chen et al. 1997; Thompson 1998; Johnson 1999; Fan 1998; Fan et al. 2000; Eckert 1999](#)). Despite the growing success of these ideas in meteorology, the oceanographic community has been slow to embrace them, and many studies of the stability of ocean flows still employ the traditional ideas, which may be limited.

In this paper the ideas of generalized linear stability theory have been applied to the wind-driven ocean circulation in the form of a barotropic double gyre in a rectangular ocean basin, a system that has been discussed extensively in the literature, and that is often used as a surrogate for the subtropical and subpolar gyre system (see [Pedlosky 1996](#) and [Chang et al. 2001](#) for excellent reviews). The double-gyre circulation is characterized by an inhomogeneous flow field with a relatively slow Sverdrup circulation in the interior of the ocean basin and swift western boundary currents that separate from the boundary and flow as a zonally oriented jet into the interior (see [Fig. 1a](#) ). It is well known from traditional stability theory that such inhomogeneities, characterized by regions of straining flow, can act as sources and sinks of energy leading to the classical notion of barotropic instability ([Pedlosky 1979](#)). For an asymptotically stable flow, there are no growing eigenmodes of barotropic instability. However, the flow field inhomogeneities do render non-normal the linear operators that describe perturbation development. Thus, the eigenmodes of the system are nonorthogonal and rapid transient perturbation growth is possible via linear eigenmode interference. This suggests that there must be sources (and sinks) of energy that, of course, are the same as those identified above. Thus, in an asymptotically stable system there is an equivalence between the energy sources and sinks and linear interference of the eigenmodes.

Our paper is laid out as follows. In [section 2](#) we explore the causes of non-normality in the barotropic vorticity equation, and discuss the equivalence between sources and sinks of physical quantities, such as energy, and the linear interference of eigenmodes. These ideas are applied to a double-gyre circulation in [section 3](#). Stochastic forcing of this same system is considered in [section 4](#) and the dynamics of stochastically induced variability is explored. [Sections 2–4](#) deal with asymptotically stable autonomous systems. In [section 5](#), nonautonomous and unstable systems are considered. We end with a summary and discussion of our results in [section 6](#).

2. The barotropic vorticity equation

The nondimensional, nonlinear, forced, barotropic vorticity equation for a flat-bottomed ocean can be written as

$$\partial\Pi/\partial t + \alpha J(\Psi, \Pi) + \partial\Psi/\partial x + \gamma\Pi = w_E, \quad (1)$$

where Ψ and Π are streamfunction and vorticity, respectively; $J(\cdot, \cdot)$ is the Jacobian operator; α is the Rossby number; γ is the nondimensional coefficient of bottom friction; and w_E is the nondimensional Ekman pumping velocity at the upper boundary. The nondimensionalization used for the examples presented in this paper is described in [appendix A](#). [Equation \(1\)](#) was solved in a rectangular domain $0 \leq x \leq 1$, $-1 \leq y \leq 1$ subject to the condition that $\Psi = 0$ along solid boundaries.

Consider small perturbations ψ to Ψ and ζ to Π . A first-order Taylor expansion of [\(1\)](#) yields

where ∇^{-2} represents the inverse Laplacian and the associated boundary condition $\Psi = \psi = 0$. Equation (2) will be referred to as the tangent linear equation.

a. Energy and enstrophy

Perturbation growth or decay is often measured in terms of the basin-integrated perturbation energy E or perturbation enstrophy Q . The equations that describe the evolution of E and Q are well known and given by

$$\frac{\partial E}{\partial t} = \underbrace{-\alpha \int_{-1}^1 \int_0^1 u' v' V_x + u' v' U_y + u'^2 U_x + v'^2 V_y dx dy}_{E_R} - \underbrace{2\gamma E}_{E_d} \quad (3)$$

$$\frac{\partial Q}{\partial t} = \underbrace{-\alpha \int_{-1}^1 \int_0^1 \zeta \mathbf{u}' \cdot \nabla \Pi dx dy}_{Q_R} - \underbrace{\frac{1}{2} \int_{-1}^1 [v'^2]_0^1 dy}_{Q_b} - \underbrace{2\gamma Q}_{Q_d}, \quad (4)$$

where $u' = -\partial\psi/\partial y$, $v' = \partial\psi/\partial x$, $U = -\partial\Psi/\partial y$, $V = \partial\Psi/\partial x$. The terms E_R and Q_R are the net perturbation energy and enstrophy source and sink terms proportional to the perturbation momentum stresses, Q_b is the net source or sink of enstrophy due to wave reflections at the western and eastern boundaries, and E_d and Q_d are energy and enstrophy dissipation. In general, individual terms of the integrand in (3) will attain their largest magnitude in regions of largest basic state strain, but they may be either positive or negative. Similarly, the individual terms of the integrand of Q_R can be of either sign and will have the largest magnitude in regions characterized by large basic state vorticity gradients. If the integrals E_R and $(Q_R + Q_b)$ are positive and exceed the size of the dissipation sinks, then growth of E and Q is possible. For an asymptotically unstable system, this is true for at least one of the eigenmodes, and the system is said to be barotropically unstable. For a non-normal, asymptotically stable system, rapid growth of E and Q is still possible due to linear interference of the nonorthogonal eigenmodes (e.g., Farrell and Ioannou 1996f). In section 2b, we will describe the conditions under which this rapid growth can occur.

Before proceeding, it is appropriate to comment on the boundary source/sink term Q_b in (4). This is a fundamental feature of the system and is due to Rossby wave reflection at the boundaries. At a western (eastern) boundary, long (short) Rossby waves reflect as short (long) Rossby waves and enstrophy is created (destroyed) (see Pedlosky 1979, his sections 3.23 and 3.27, or Rhines 1977, his section 7). Here, Q_b describes the result of this process, and its physical interpretation depends on the form of dissipation and the boundary conditions imposed at the solid boundaries. The linear, inviscid form of the enstrophy equation can be written as $\partial(\zeta^2/2)/\partial t + \nabla \cdot \mathbf{f}_Q = 0$ where $\mathbf{f}_Q = \mathbf{i}\beta(\mathbf{v}'^2 - u'^2)/2 - \mathbf{j}\beta u' \mathbf{v}'$ is the enstrophy flux. Integrating this equation over the basin subject to the condition of no normal flow at the solid boundaries yields Q_b as defined in (4), showing that Q_b represents the net flux of enstrophy through the western and eastern boundaries. If eddy viscosity $\kappa \nabla^2 \zeta$ is added to the rhs of (2) then $Q_b = -\int_{-1}^1 \frac{1}{2} (\mathbf{v}'^2)_0^1 dy + \int_{-1}^1 (\kappa \zeta^2 / \partial x)_0^1 dy + \int_0^1 \frac{1}{2} (\kappa \zeta^2 / \partial y)_{-1}^1 dx$, where κ is the nondimensional coefficient of eddy viscosity. The last two terms also represent a flux of enstrophy at the boundaries. In this case an additional boundary condition is required to solve (2). If we choose a no-slip condition, the first term in Q_b vanishes. If we choose a slip condition, $\zeta = 0$ at the boundary and the flux terms $\kappa \zeta^2 / \partial x$ and $\kappa \zeta^2 / \partial y$ vanish. Similar arguments can be applied if higher order dissipation is included. In any case, there will be a nonzero boundary flux of Q represented by Q_b , which is a fundamental and inescapable consequence of the Rossby wave reflection process.

b. Non-normality

We will consider a discrete form of the tangent linear equation since this simplifies the resulting algebraic analysis, and because all examples presented in subsequent sections were solved numerically (see appendix A). Consider a grid of $M \times N$ regularly spaced points in the domain $x = 0, M\Delta x$, $y = 0, N\Delta y$, where $\Delta x = 1/M$ and $\Delta y = 2/N$. The discrete form of (2) will be represented as

$$\begin{aligned} \partial \zeta / \partial t + \alpha \mathbf{J}_{\Psi_x} \mathbf{D}_y \zeta - \alpha \mathbf{J}_{\Psi_y} \mathbf{D}_x \zeta + \alpha \mathbf{J}_{\Pi_y} \mathbf{D}_x \mathbf{L}^{-1} \zeta \\ - \alpha \mathbf{J}_{\Pi_x} \mathbf{D}_y \mathbf{L}^{-1} \zeta + \mathbf{D}_x \mathbf{L}^{-1} \zeta + \gamma \mathbf{I} \zeta = 0, \end{aligned} \quad (5)$$

where ζ is the vector of MN grid point values of relative vorticity. If $x = a\Delta x$ and $y = b\Delta y$ where a and b are integers then

$\zeta(x, y)$ represents the k th element of ζ where $k = (b-1)M + a$ and ranges from 1 to MN . The matrices \mathbf{D}_r and \mathbf{L} are the discrete analogues of $\partial/\partial r$ and ∇^2 respectively, and $\mathbf{J}_{\Phi_r} = \text{diag}(\partial\Phi_i/\partial r)$ where Φ_i are the elements of the vector Φ . We can also write (5) as $\partial\zeta/\partial t = \mathbf{A}\zeta$, where the definition of \mathbf{A} immediately follows. In section 2d, we will consider only cases for which \mathbf{A} is autonomous and asymptotically stable.

It is the commutative properties of \mathbf{A} with its adjoint that determines the non-normal character of the system. The exact form of the adjoint tangent linear vorticity equation depends on the inner-product used to define the scalar product of two vectors. To illustrate this important point, we will restrict our attention to the L2-norm and rewrite equation (5) as

$$\frac{\partial \mathbf{v}}{\partial t} = \mathbf{M}^T \mathbf{A} \mathbf{M}^T \mathbf{v} = \mathbf{C} \mathbf{v}, \quad (6)$$

where $\mathbf{X} = \mathbf{M} \mathbf{M}^T$ is symmetric positive definite, $\mathbf{v} = \mathbf{M}^T \zeta$ and $\mathbf{C} = \mathbf{M}^T \mathbf{A} \mathbf{M}^T$. Consider the scalar product of some arbitrary real vector ϕ with \mathbf{v} given by $\phi^T \mathbf{v}$. If $\phi = \mathbf{v}$, then the scalar product defines the L2-norm $\mathcal{N} = \mathbf{v}^T \mathbf{v} = \zeta^T \mathbf{X} \zeta$. The scalar product of the arbitrary vector ϕ with (6) yields $\phi^T \partial \mathbf{v} / \partial t = \phi^T \mathbf{C} \mathbf{v}$. Using the chain rule on the lhs and rearranging the rhs, we have $\partial(\phi^T \mathbf{v}) / \partial t - \mathbf{v}^T \partial \phi / \partial t = \mathbf{v}^T \mathbf{C}^T \phi$. Thus for arbitrary \mathbf{v} , we obtain

$$-\frac{\partial \phi}{\partial t} = \mathbf{C}^T \phi = \mathbf{M}^{-1} \mathbf{A}^T \mathbf{M} \phi, \quad (7)$$

providing $\partial(\phi^T \mathbf{v}) / \partial t = 0$, which is a necessary condition for solutions of (6) and (7). Equation (7) is the adjoint vorticity equation with respect to the innerproduct that defines the norm \mathcal{N} . If $\mathbf{X} = \mathbf{I}$, then $\mathcal{N} = Q$ and (7) becomes the adjoint equation with respect to the enstrophy norm. If $\mathbf{X} = -\mathbf{L}^{-1}$, then $\mathcal{N} = E$ and (7) becomes the adjoint equation with respect to the energy norm. The non-normality of the system, which depends on the commutative properties of \mathbf{C} and \mathbf{C}^T using the appropriate choice of \mathbf{X} , determines whether or not E and Q can grow in an asymptotically stable system.

By way of an example, consider for a moment a zonally oriented channel that is periodic in x and bounded in y with $\Psi = \Psi(y)$. In this case $\mathbf{A} = \alpha \mathbf{J}_{\Psi_y} \mathbf{D}_x - \alpha \mathbf{J}_{\Pi_y} \mathbf{D}_x \mathbf{L}^{-1} - \mathbf{D}_x \mathbf{L}^{-1} - \gamma \mathbf{I}$, and the transpose of \mathbf{A} is given by $\mathbf{A}^T = -\alpha \mathbf{D}_x \mathbf{J}_{\Psi_y} + \alpha \mathbf{L}^{-1} \mathbf{D}_x \mathbf{J}_{\Pi_y} + \mathbf{L}^{-1} \mathbf{D}_x - \gamma \mathbf{I}$ where use is made of the fact that $\mathbf{D}_r^T = -\mathbf{D}_r$, $\mathbf{J}_{\Phi_r}^T = \mathbf{J}_{\Phi_r}$, and $\mathbf{L}^{-1T} = \mathbf{L}^{-1}$. For a periodic domain \mathbf{D}_x and \mathbf{L}^{-1} commute, and the \mathbf{J}_{Φ_r} commute with each other since they are diagonal. However, \mathbf{J}_{Φ_r} does not commute with \mathbf{D}_x , therefore $[\mathbf{C}, \mathbf{C}^T] = \mathbf{C} \mathbf{C}^T - \mathbf{C}^T \mathbf{C} \neq 0$ for either $\mathbf{X} = \mathbf{I}$ or $\mathbf{X} = -\mathbf{L}^{-1}$, and growth of Q and E is possible. If, on the other hand, streamfunction is a linear function of latitude such that $\Psi(y) = \Psi_0 y$ where Ψ_0 is a constant, then $\mathbf{J}_{\Psi_y} = \Psi_0 \mathbf{I}$, $\mathbf{J}_{\Pi_y} = 0$ and $[\mathbf{C}, \mathbf{C}^T] = 0$. In this special case, \mathbf{C} is a normal operator, and since the strain Ψ_{yy} vanishes, E_R and Q_R in (3) and (4) both vanish so neither E or Q can grow.

In the general case of a bounded ocean basin with $\Psi = \Psi(x, y)$, \mathbf{C} is non-normal for both $\mathbf{X} = \mathbf{I}$ and $\mathbf{X} = -\mathbf{L}^{-1}$. Thus, the eigenmodes are non-orthogonal with respect to the Q norm and E norm, and transient growth of Q and E is possible. The sources and sinks of E and Q are E_R , Q_R and Q_b in (3) and (4).

c. The equivalence of source/sink terms and eigenmode interference

If perturbation growth occurs as measured by some norm \mathcal{N} there must be a net source of the quantity \mathcal{N} within the domain. Therefore, in a non-normal, asymptotically stable system there is an equivalence between the sources of \mathcal{N} and the process of linear eigenmode interference. The nature of the \mathcal{N} -source terms is revealed by examining the evolution equation for $\mathcal{N} = \zeta^T \mathbf{X} \zeta$:

$$\partial \mathcal{N} / \partial t = \zeta^T \mathbf{M} (\mathbf{M}^T \mathbf{A} \mathbf{M}^T \mathbf{T}^{-1} + \mathbf{M}^{-1} \mathbf{A}^T \mathbf{M}) \mathbf{M}^T \zeta. \quad (8)$$

If \mathbf{E} is the matrix whose columns are the eigenvectors $\hat{\mathbf{S}}_k$ of \mathbf{A} and $\Omega = \text{diag}(\sigma_k)$ is the matrix of associated eigenvalues σ_k , then $\zeta(t) = \mathbf{E} e^{\Omega t} \mathbf{a}$ where $\mathbf{a} = \mathbf{E}^{-1} \zeta(0) = (a_k)$ is the vector of eigenmode amplitudes a_k . Equation (8) can then be written in the equivalent form:

where superscript H denotes the Hermitian transpose, superscript $*$ denotes the complex conjugate, and $\mathbf{U} = \Omega e^{\Omega t} \mathbf{a} \mathbf{a}^H e^{\Omega^H t}$. In deriving (9), repeated use is made of the identity $\text{tr}\{\mathbf{ABC}\} = \text{tr}\{\mathbf{BCA}\} = \text{tr}\{\mathbf{CAB}\}$ where \mathbf{A} , \mathbf{B} and \mathbf{C} are matrices of appropriate dimensions. Equation (9) shows how the linear eigenmode interferences $\mathbf{E}^H \mathbf{X} \mathbf{E}$ influence the evolution of \mathcal{N} . Therefore, the source/sink terms that appear in (8) also represent the collective effect of the linear interference of eigenmodes represented by $\hat{\mathbf{S}}_j^H \mathbf{X} \hat{\mathbf{S}}_j e^{(\sigma_j + i\sigma_j^*)t}$ in (9).

For $\mathcal{N} = E$ the source/sink terms E_R and E_d in (3) are analogous to the quadratic terms on the rhs of (8). Similarly, for $\mathcal{N} = Q$ the rhs of (4) is equivalent to the rhs of (8). Thus, the net effect of the perturbation stress-related source and sink terms, boundary terms and dissipation terms are also equivalent to linear eigenmode interference according to the rhs of (9). This demonstrates that the traditional notion of barotropic growth and decay of perturbations can also be viewed geometrically in terms of linear eigenmode interference. Recall that the source/sink terms of E_R and Q_R in (3) and (4) are due to the straining component of the flow. However, it is the very existence of strain that is responsible for the nonorthogonality of the eigenmodes and which permits perturbation growth via linear interference of the eigenmodes.

3. A double gyre basic-state circulation

The ideas of section 2 were applied to a wind-driven double gyre ocean circulation in a rectangular barotropic ocean. As described in appendix A, Eq. (1) was solved numerically for both high and low horizontal resolutions. Results from the high resolution model will be presented primarily in sections 3 and 4, while the low-resolution model will be used in section 5 due to its computational efficiency. A zonally uniform surface Ekman pumping velocity given by $w_E(y) = w_0 \sin(\pi y)$ was used in (1) where $w_0 = 1$ and corresponds to an amplitude of $4.31 \times 10^{-6} \text{ m s}^{-1}$ typical of the average value deduced from observed winds over the subtropical gyre of the North Atlantic (Hellerman and Rosenstein 1983). A steady double gyre develops in response to the forcing as shown in Fig. 1a for the high-resolution model.

We will consider autonomous perturbation growth as described by the tangent linear Eq. (5) linearized about the steady, asymptotically stable circulation appropriate for the model used (i.e., Fig. 1a for the high-resolution model). All of the calculations described in subsequent sections were performed using the model described in appendix A, and using the algorithms outlined in appendix B.

a. Non-normality and pseudospectra

The non-normality of a dynamical system can be explored and quantified by considering the solution of (5) subject to a forcing of constant complex frequency $\omega = \omega_r + i\omega_i$, and plotting contours of the norm of the resolvent $\|\mathcal{R}(\omega)\| = \|(\omega \mathbf{I} - \mathbf{C})^{-1}\|$, where $\mathbf{C} = \mathbf{M}^T \mathbf{A} \mathbf{M}^T$ is defined by (6). The norm of $\mathcal{R}(\omega)$ provides an upper bound on the ratio of the size of the system response (i.e., $\|\zeta(t)\|$) to the size of the forcing. We have used the L2-norm to compute $\|\mathcal{R}(\omega)\|$, thus if $\mathbf{X} = \mathbf{M} \mathbf{M}^T = \mathbf{I}$ the L2-norm is equivalent to the enstrophy norm Q . Following Trefethen (1996),

$$1/\text{dist}(\omega, \Lambda(\mathbf{C})) \leq \|\mathcal{R}(\omega)\| \leq \kappa(\mathbf{E})/\text{dist}(\omega, \Lambda(\mathbf{C})), (10)$$

where $\text{dist}(\omega, \Lambda(\mathbf{C}))$ is the distance function and represents the shortest distance in the complex plane between ω and the spectrum of eigenvalues of \mathbf{C} denoted $\Lambda(\mathbf{C})$, and $\kappa(\mathbf{E})$ is the condition number of the matrix of eigenvectors \mathbf{E} of \mathbf{C} . For a normal system $\kappa(\mathbf{E}) = 1$ and (10) reduces to an equality.

For a non-normal system $\kappa(\mathbf{E}) > 1$ and contours of $\|\mathcal{R}(\omega)\|$ differ from those of the inverse distance function. Equation (10) provides an upper bound on $\|\mathcal{R}(\omega)\|$. Figure 2a shows a large portion of the eigenspectrum of (5) for the high-resolution model linearized about the double gyre circulation of Fig. 1a. As explained later, of primary interest is the portion of the spectrum in the vicinity of the origin, which is illustrated in more detail in Fig. 2b. Figure 2b also shows contours of $\|\mathcal{R}(\omega)\|$ for (5) linearized about the steady wind-driven circulation of Fig. 1a. Recall that $\Lambda(\mathbf{A}) = \Lambda(\mathbf{C})$, and that if $\hat{\mathbf{S}}_k$ are the eigenvectors of \mathbf{A} then the eigenvectors of \mathbf{C} are $\mathbf{M}^T \hat{\mathbf{S}}_k$. We assume that eigensolutions of (5) are proportional to $e^{\sigma t}$ where $\sigma = \sigma_r + i\sigma_i$ is the complex eigenfrequency with real and imaginary components σ_r and σ_i respectively. Thus if $\sigma_r < 0$ for all eigenmodes the system is asymptotically stable. The eigenspectra of Figs. 2a,b confirm that the double gyre circulation of Fig. 1a is asymptotically stable. Figure 2b shows that contours of $\|\mathcal{R}(\omega)\|$ differ considerably from contours of $1/\text{dist}(\omega, \Lambda(\mathbf{C}))$.

The set of all complex frequencies ω for which $\|\mathcal{R}(\omega)\| \geq \epsilon^{-1}$ is called an ϵ -pseudospectrum (Trefethen et al. 1993) and is denoted $\Lambda_\epsilon(\mathbf{C})$. For each contour value $c = \epsilon^{-1}$ plotted in Fig. 2b, the largest value of ω_r that is found on each contour (indicated by an asterisk in Fig. 2b for selected contours) exceeds c^{-1} [i.e., $\sup_{\omega \in \Lambda_\epsilon(\mathbf{C})} \text{Re}(\omega) > \epsilon$]. According

to the Hille–Yosida theorem (Reddy et al. 1993), this indicates that transient growth of Q must be possible. The potential for transient growth of perturbations is quantified by norm of the propagator $\|e^{\mathbf{C}t}\|$ which is plotted in Fig. 2c for the Q norm as a function of the time interval t , and as anticipated transient growth is possible over a wide range of time intervals. The spatial structure of the perturbations associated with the fastest transient growth for each time interval are the fastest growing singular vectors discussed in the next section.

In principle, pseudospectra can also be computed for the E norm by choosing $\mathbf{X} = -\mathbf{L}^{-1}$. However in practice this is computationally very demanding for the high-resolution model due to the repeated use of the factorization $\mathbf{X} = \mathbf{M}\mathbf{M}^T$. Pseudospectra have been calculated for the low resolution model for both the Q and E norms and reveal that they are qualitatively very similar to each other (not shown). In addition, the pseudospectra of the high- and low-resolution models are qualitatively very similar for the Q norm. Therefore we anticipate that the pseudospectra of the E norm in the high-resolution model will be qualitatively similar to that in Fig. 2b, indicating that transient growth of E is possible also. This is confirmed in Fig. 2d, which shows $\|e^{\mathbf{C}t}\|$ versus t for the E norm.

The non-normality of (5) can also be quantified in terms of the linear dependence of its eigensolutions (Farrell and Ioannou 1996f). If we denote by $\hat{\mathbf{r}}_k$ the eigenmodes of \mathbf{A}^T , then the eigenmodes $\mathbf{M}^{-1}\hat{\mathbf{r}}_k$ of \mathbf{C}^T are biorthogonal to all of the eigenmodes $\mathbf{M}^T\hat{\mathbf{s}}_i$ of \mathbf{C} except for eigenmode $\mathbf{M}^T\hat{\mathbf{s}}_k$ with the corresponding complex conjugate eigenvalue. The quantity $v_k = |\mathbf{M}^T\hat{\mathbf{s}}_k| |\mathbf{M}^{-1}\hat{\mathbf{r}}_k| / (\hat{\mathbf{r}}_k^H \mathbf{X} \hat{\mathbf{s}}_k)$ is therefore a useful measure of the linear dependence of $\hat{\mathbf{s}}_k$ on the remaining members of the eigenspectra (Farrell and Ioannou 1993f) with large v_k indicating a high degree of linear dependence. The distance function in (10) shows that $|\mathcal{R}(\omega)|$ in Fig. 2b is determined by a particular subset of the eigenspectrum Λ , and this subset we will denote as Λ_c . If ω_i denotes any purely imaginary frequency, then Λ_c is the set of eigenmodes with largest σ_r for which $\omega_i \in \text{Im}(\Lambda)$. The set Λ_c is indicated in Fig. 2b by triangles. The eigenmodes that comprise Λ_c are typically the least damped within any frequency interval $\omega_i \rightarrow \omega_i + \Delta$. Figure 2e shows $\ln|v_k|$ vs σ_i for the set of eigenmodes Λ_c for the case $\mathbf{X} = \mathbf{I}$. The largest values of $|v_k|$ typically correspond to low-frequency eigenmodes.

b. Singular vectors

Solutions of (5) for an autonomous basic state can be written in the form $\zeta(t) = \mathbf{R}(t)\zeta(0)$, where $\mathbf{R} = e^{\mathbf{A}t}$ is the propagator. The initial structures of the perturbations of (5) that maximise the growth of a chosen norm $\mathcal{N} = \zeta^T \mathbf{X} \zeta$ over the time interval τ (the “optimal growth time”) are the eigenvectors of $\mathbf{R}^T(\tau)\mathbf{X}\mathbf{R}(\tau)$, which are the right singular vectors of $\mathbf{M}^T\mathbf{R}(\tau)$. The singular vectors that maximize the growth of Q and E for $\tau = 14$ days in the high-resolution model are shown in Figs. 1b and 1c, respectively. The structures of ζ and ψ for these two singular vectors are very similar. A 14-day period corresponds to the time interval that produces the largest growth factor for both Q and E as shown in Figs. 2c,d. The basic state flow in Fig. 1a is asymptotically stable. However, Figs. 1b,c indicate that in the presence of a straining basic state flow, transient growth of both E and Q is possible due to the non-normality of the system. [For a resting basic state, growth of Q is still possible due to Rossby wave reflections via Q_b in (4).]

If we denote the initial structure of the fastest growing singular vector in Fig. 1b as $\zeta(0) = \sum_k a_k \hat{\mathbf{s}}_k$ as in (9) where $\hat{\mathbf{s}}_k$ are the eigenmodes of \mathbf{A} , then Fig. 2f shows $\ln|v_k|$ versus $|a_k|$ for the subset of eigenmodes Λ_c for the case $\mathbf{X} = \mathbf{I}$. Figures 2e,f reveal that the eigenvectors onto which the singular vector projects the most (i.e., largest $|a_k|$) are also some of the most non-normal, least damped members of the eigenspectrum.

c. Stochastic optimals

The response of a non-normal system to stochastic forcing is of considerable interest because the forcing can act as a continuous source of perturbations, and linear eigenmode interference can elevate the stochastically induced variability by producing transient perturbation growth. If this variability is measured in terms of the norm \mathcal{N} , then for an asymptotically stable system, a statistically steady state is reached in which there is a balance between the input of \mathcal{N} by the forcing, dissipation of \mathcal{N} , and sources of \mathcal{N} due to straining and shearing flows. If the sources of \mathcal{N} are large, then the variability maintained by the stochastic forcing may be large. The patterns of stochastic forcing that are most effective for inducing variability in such a system are the stochastic optimals (Kleeman and Moore 1997) or forcing orthogonal functions (Farrell and Ioannou 1993f).

The stochastically forced tangent linear vorticity equation linearized about the double-gyre circulation in Fig. 1a can be written as

$$\partial\zeta/\partial t = \mathbf{A}\zeta + \mathbf{f}(t), \quad (11)$$

where \mathbf{A} is given by (5), and \mathbf{f} is the stochastic forcing vector. If (11) is discretized in time as described in Kleeman and Moore (1997) and the covariance of $\mathbf{f}(t)$ is separable in space and time, then the stochastic optimals are the eigenvectors of

$$\mathbf{Z} = \Delta t^2 \sum_{j=0}^{n-1} \sum_{m=0}^{n-1} D_{m,j} \mathbf{R}_{j+1,n-1}^T \mathbf{X} \mathbf{R}_{m+1,n-1}, \quad (12)$$

where Δt is the time step, the summations represent integrals in time, $\mathbf{R}_{i,j}$ is the propagator matrix for the time interval $t = [i\Delta t, j\Delta t]$, \mathbf{X} is as defined earlier, and $D_{m,j}$ describes the temporal correlation of \mathbf{f} .

The eigenvalues and eigenvectors of \mathbf{Z} will be denoted s_i and \mathbf{S}_i , respectively. [Figure 3](#) shows the patterns of Ekman pumping velocity associated with the first six members of the stochastic optimal spectrum of the high resolution model for the double-gyre circulation of [Fig. 1a](#) computed using an enstrophy norm [$\mathbf{X} = \mathbf{I}$ in (12)], a time interval of 300 days, and assuming a forcing $\mathbf{f}(t)$ in (11) that is white in time, in which case $D_{m,j} = \delta_{m,j}/\Delta t$. The structures of the stochastic optimals do not vary for time intervals greater than 150 days or so. The eigenvalues of the first 20 members of the stochastic optimal spectrum are shown in [Fig. 4](#), which reveals that the eigenvector in [Fig. 3a](#) dominates the spectrum. If \mathbf{f} were composed of each member of the stochastic optimal spectrum such that each \mathbf{S}_i contributes equally to the enstrophy input by the forcing, then the fraction of stochastically induced variance explained by \mathbf{S}_i is $s_i/\text{tr}(\mathbf{Z})$ (Farrell and Ioannou 1993f; Kleeman and Moore 1997). Evaluating $\text{tr}(\mathbf{Z})$ for the high resolution model is computationally prohibitive, but is possible for the low resolution model. [Figure 4](#) shows $s_i/\text{tr}(\mathbf{Z})$ for the first 20 members of the stochastic optimal spectrum of the low resolution model (linearized about the double gyre solution of that model), and reveals that \mathbf{S}_1 would explain $\sim 65\%$ of the forcing-induced variance in this model. The stochastic optimals of the low-resolution model are qualitatively similar to those shown in [Fig. 3](#). [Figure 4](#) reveals that the shape of the stochastic optimal spectra are very similar in the two models, thus \mathbf{S}_1 in [Fig. 3a](#) will explain by far the largest fraction of stochastically induced variance in the high-resolution model as well.

Calculations (not shown) reveal that the structures of the stochastic optimals in [Fig. 3](#) are essentially unchanged when the energy norm ($\mathbf{X} = -\mathbf{L}^{-1}$) is used. There is no restriction on the temporal nature of the forcing \mathbf{f} in (11), and further calculations reveal that the structure of the gravest stochastic optimal \mathbf{S}_1 in [Fig. 3a](#) is insensitive to the decorrelation time of the stochastic forcing (not shown).

4. Stochastically induced variability

In this section the preceding ideas are used to explore the response of the wind-driven ocean circulation to stochastic forcing, a problem that has attracted considerable attention in the oceanographic literature (see Moore 1999 for a review). Consider the barotropic vorticity [equation \(1\)](#) subject to surface Ekman pumping:

$$\frac{\partial \Pi}{\partial t} + \alpha J(\Psi, \Pi) + \frac{\partial \Psi}{\partial x} = -\gamma \Pi + \overline{w'_E} + w'_E, \quad (13)$$

where $\overline{w'_E}$ represents the deterministic (i.e., predictable) component of the surface Ekman pumping and w'_E is the stochastic (i.e., unpredictable) component. Observations indicate that at middle and high latitudes $|w'_E| \sim |\overline{w'_E}|$ (Willebrand 1978; Chave et al. 1991; Samelson and Shroyer 1991) so the response of the ocean circulation to both deterministic and stochastic forcing is clearly of interest. In the following, the deterministic component of the forcing is given by $\overline{w'_E} = w_0 \sin(\pi y)$, where $w_0 = 1$ and is the forcing used to generate the steady two-gyre circulation of [Fig. 1a](#).

The stochastic component of the Ekman pumping w'_E was constructed from a linear super-position of the first 20 stochastic optimals \mathbf{S}_i of the circulation in [Fig. 1a](#), assuming a temporal decorrelation time of 4 days, so that

$$w'_E = \sum_{i=1}^N b_i(t) \mathbf{S}_i, \quad (14)$$

where $N = 20$. The total number of stochastic optimals for the model domain considered here is 5995. If each of these \mathbf{S}_i contribute equally to the enstrophy input by the stochastic forcing w'_E , then based on the low-resolution model, the first 20 members of the stochastic optimal spectrum will most likely explain more than 90% of the stochastically induced enstrophy variability (cf. [Fig. 4](#)). The amplitude functions $b_i(t)$ were constructed from a lag-1 autoregressive [AR(1)] model of the form:

$$b_i(t_{j+1}) = k b_i(t_j) + \xi_{i,j}, \quad (15)$$

where $\langle b_i^2(t) \rangle$ has the same value for all i , and $k = 0.911$, which yields a temporal decorrelation time of 4 days using a

white noise input $\xi_{i,j}$. The stochastic forcing w'_E has the properties $\langle w'_E \rangle = 0$ and $(\langle w'^2_E \rangle)^{1/2} = \rho w_0$ where the amplitude coefficient ρ was varied. In keeping with [section 3c](#), it was assumed that the stochastically induced variability will be described by the tangent linear form of [\(1\)](#) [cf. [Eq. \(5\)](#)] subject to the stochastic forcing w'_E [cf. [Eq. \(11\)](#)]. The validity of this assumption is considered next.

a. Validity of the tangent linear assumption

The validity of the tangent linear assumption was explored in the following way. Two integrations of the high-resolution nonlinear model were performed: (i) with \bar{w}_E as given above and $w'_E = 0$, and (ii) with \bar{w}_E as given above and w'_E given by [\(14\)](#) and [\(15\)](#). The differences $\Delta\Pi$ and $\Delta\Psi$ between the two model solutions were computed, and time series of $\Delta E = -\int_{-1}^1 \int_0^1 \Delta\Psi \Delta\Pi \, dx \, dy$, $\Delta Q = \int_{-1}^1 \int_0^1 \Delta\Pi^2 \, dx \, dy$, and $\Delta P = \int_{-1}^1 \int_0^1 \Delta\Psi^2 \, dx \, dy$ are shown in [Fig. 5](#) for $\rho = 0.1$ and $\rho = 1.0$. The high-resolution tangent linear model linearized about the non-linear solution arising from \bar{w}_E used in (i) (cf. [Fig. 1a](#)) was run using the identical stochastic forcing w'_E to that used in (ii). Time series of E , Q and $P = \int_{-1}^1 \int_0^1 \Psi^2 \, dx \, dy$ from the tangent linear model are shown in [Fig. 5](#) also. [Figures 5a,b,c](#) show that for low-amplitude stochastic forcing (i.e., $\rho = 0.1$) the time series from the two models are indistinguishable. For higher levels of stochastic forcing ($\rho = 1.0$), the time series of E and ΔE , and P and ΔP track each other very well. The trends in Q and ΔQ are essentially the same, but the tangent linear model over estimates the amplitudes of the peaks in Q . To illustrate this further, [Figs. 5g-j](#) show snapshots of $\Delta\Psi$, $\Delta\Pi$, Ψ and ζ on day 330 for the case $\rho = 1.0$. This is a time at which Q and ΔQ disagree considerably as revealed by [Fig. 5e](#). [Figures 5g,h](#) show that the perturbation streamfunction fields are very similar, both in terms of spatial structure and amplitude. The perturbation vorticity of the tangent linear model ([Fig. 5i](#)), however, has a larger amplitude than in the nonlinear model ([Fig. 5j](#)). The amplitude of vorticity perturbations is suppressed in the nonlinear model by the perturbation interactions described by $\mathcal{K}(\Psi, \zeta)$. The structure of these stochastically induced perturbations will be explored in more detail in [section 4b](#). By and large, however, the overall structure of the vorticity perturbations in the two models are in reasonable agreement.

We note that the validity of the tangent linear assumption is also a function of the proximity of the circulation to its primary bifurcation point. [Figures 2a,b](#) indicate that the circulation in [Fig. 1a](#) is not close to the bifurcation point in this case, and the tangent linear assumption is rather good even for $\rho = 1.0$. Other experiments (not shown) suggest that as the bifurcation point is approached from the stable side, the tangent linear assumption breaks down for $\rho \sim 1$ but is still valid for moderate stochastic forcing amplitudes $\rho \sim 0.3$. For $\rho \sim 1$ the model undergoes aperiodic transitions between asymmetric double-gyre circulation states much like the case discussed by [Sura et al. \(2000\)](#).

b. The dynamics of stochastically induced variability

[Figure 5](#) indicates that the tangent linear assumption can be used to understand the dynamics of stochastically induced variability in the wind-driven ocean circulation for the present case. Since each stochastic optimal contributes equally to the enstrophy input by the stochastic forcing in [\(14\)](#), then according to [Fig. 4](#), \mathbf{S}_1 will explain by far the largest fraction of the stochastically induced variance in [Fig. 5](#). This is confirmed in [Fig. 6](#), which shows timeseries of E and Q from the stochastically forced tangent linear model when $w'_E = b_1(t)\mathbf{S}_1$ and when $w'_E = \sum_{i=2}^{20} b_i(t)\mathbf{S}_i$ where the $b_i(t)$ are identical to those of the previous experiment.

The stochastic optimal \mathbf{S}_1 ([Fig. 3a](#)) has a structure very similar to the fastest growing singular vector ([Fig. 1b](#)). Therefore \mathbf{S}_1 will induce perturbations in the flow that grow rapidly. [Figures 2e,f](#) reveal that the fastest growing singular vector projects most of all onto some of the most non-normal, least-damped eigenmodes of the system. [Figure 2b](#) reveals that the least-damped eigenmode has a decay rate of $3.1 \times 10^{-2} \text{ day}^{-1}$ and is nonoscillating. The vorticity structure of this eigenmode is shown in [Fig. 7a](#), and is similar to the stochastically induced perturbation vorticity in [Fig. 5i](#). The optimal excitation for this eigenmode, which maximizes the growth of $\mathcal{N} = \zeta^T \mathbf{M} \mathbf{M}^T \zeta$, is the corresponding adjoint eigenmode $\mathbf{M}^{-1} \hat{\zeta}$ ([Farrell 1988a](#)). [Figure 7b](#) shows the optimal excitation of the eigenmode in [Fig. 7a](#) relative to the Q norm. Clearly \mathbf{S}_1 will induce perturbations that will project significantly onto the least-damped adjoint eigenmode, which in turn will evolve into the least damped eigenmode. This is qualitatively what [Fig. 5i](#) suggests.

To illustrate this idea further, [Fig. 8](#) shows the time evolution in the tangent linear model of a perturbation with an initial vorticity structure identical to \mathbf{S}_1 . The initial basin-scale structure of the perturbation is quickly replaced by smaller-scale structures confined to the basic-state western boundary currents and their eastward extension. [Figure 8](#) shows that this occurs very quickly in the case of ζ , and the structure of the least-damped eigenmode is clearly visible after 5 days ([Fig. 8g](#)). By day 15, [Fig. 8h](#) is reminiscent of the stochastically induced perturbation in [Fig. 5i](#). The evolution of the perturbation in [Fig. 8](#) can be understood by examining the sources of E and Q , that arise from non-normality in the system, described by [\(3\)](#) and [\(4\)](#). Here, E_R is large in regions where the basic-state strain is large, while Q_R is large in regions where the gradients of the basic state vorticity are large. Both of these conditions are satisfied in the western boundary currents and where they separate from the boundary and flow east ([Figs. 8a and 8e](#)). [Figure 8i](#), which shows time series of E_R , Q_R and Q_b , indicates that E_R and Q_R dominate over the boundary sources and sinks.

In [section 2c](#) the equivalence between the source/sink terms E_R and Q_R and linear eigenmode interference was discussed.

We will now explore these equivalent interpretations of the dynamics of perturbation growth for the case shown in [Fig. 8](#)

The structure of \mathbf{S}_1 is similar in many respects to the fastest growing singular vector of the Q norm for a resting basic state (not shown), and the latter can be represented as a linear superposition of the basin modes¹ of a resting ocean. Thus the evolution of a perturbation with the structure of \mathbf{S}_1 shown in [Fig. 8](#) can also be conveniently explored in terms of the basin modes and their interaction with the double gyre circulation. It is easy to show that basin modes with identical meridional wavenumber but different zonal wave numbers are not orthogonal with respect to the enstrophy norm, which according to [section 2c](#), means that a source of enstrophy is present [cf. Q_b in (4)]. A perturbation with the structure of \mathbf{S}_1 projects primarily onto the basin modes with meridional wave number $\pi/2$. The projection of \mathbf{S}_1 on these basin modes is shown in [Fig. 9n](#) as a function of the zonal wavenumber, and indicates that \mathbf{S}_1 has largest projection on the lowest zonal wavenumber basin mode. One phase of this basin mode is shown in [Fig. 9e](#). The evolution of the basin mode in [Fig. 9e](#) in the high-resolution tangent linear model linearized about the double gyre circulation is shown in [Fig. 9f](#) after 15 days. Note that [Fig. 9f](#) is an expanded view of the region where the western boundary currents separate from the coast and flow east ([Figs. 9h,i,k,l](#) represent fields in the same subregion). Apart from a longer zonal fetch, [Fig. 9f](#) is similar to [Figs. 8h](#) and [5i](#), and is remarkably similar to the least-damped eigenmode in [Fig. 7a](#). The difference in zonal scale can be accounted for by the addition of other basin modes with larger zonal wavenumbers (see below). Time series of Q_R and E_R are shown in [Fig. 9g](#) for the evolving basin mode, and indicate that Q and E are liberated from the basic state by perturbation fluxes.

Each basin mode of a resting ocean can be represented as the linear superposition of two long and two short plane parallel Rossby waves ([Pedlosky 1965](#) and [1979](#), his section 3.25). These will be referred to as LRW1, LRW2, SRW1, and SRW2, respectively. The four Rossby waves that make up the basin mode of [Fig. 9e](#) are shown in [Figs. 9a-d](#). The evolution of LRW1 and SRW1 in the tangent linear model linearized about the double-gyre circulation is shown in [Figs. 9h and 9i](#) after 15 days (LRW2 and SRW2 evolve in a similar way). A comparison of these with [Fig. 9f](#) indicates that the gravest basin mode structure at this time is primarily due to the interaction of the short Rossby waves with the basic-state flow. Time series of Q_R and E_R for these experiments are shown in [Fig. 9j](#) and reveal that SRW1 liberates more Q and E from the basic state than LRW1 (and similarly for SRW2 and LRW2).

The source term Q_R of (4) is composed of two terms, $-\alpha \zeta u' \Pi_x$ and $-\alpha \zeta v' \Pi_y$, where Π_y is approximately an order of magnitude larger than Π_x over the entire domain, and has its largest values in the western boundary current separation region as shown in [Fig. 9k](#). For LRW1 and LRW2 $|u'| \gg |v'|$ while for SRW1 and SRW2 $|v'| \gg |u'|$ as illustrated in [Figs. 9a-d](#). Combined with the fact that $\Pi_y > \Pi_x$, the dominant term in Q_R is $-\alpha \zeta v' \Pi_y$, which arises primarily from the interaction of the short Rossby waves with the basic-state flow. [Figure 9l](#) shows $-\zeta v' \Pi_y$ for SRW1 at $t = 0$, and indicates growth of Q along the basic-state jet axis since here $\Pi_y > 0$ ([Fig. 9k](#)) and v' and ζ are of opposite sign during some wave phases ([Figs. 9c,d](#)) rendering $-\zeta v' \Pi_y > 0$. The spatial structure of $-\zeta v' \Pi_y$ in [Fig. 9l](#) is similar to [Fig. 9f](#), the evolved basin mode, and the least-damped eigenmode of the double-gyre circulation in [Fig. 7a](#). This analysis indicates therefore that the least-damped eigenmode of the double-gyre circulation in [Fig. 7a](#) is a direct result of the interaction of the short Rossby waves with the basic-state flow.

[Figure 9n](#) reveals that \mathbf{S}_1 has a significant projection on other basin modes with larger zonal wavenumbers than that considered above. In the presence of the double-gyre circulation, these basin modes and their associated component plane parallel Rossby waves behave in a qualitatively similar way to that described in [Figs. 9e-l](#). However, as the zonal wavenumber increases the flow associated with the long (short) Rossby waves becomes progressively more zonal (meridional) enhancing the source term $-\zeta v' \Pi_y$. The increase in zonal wavenumber leads to the appearance of additional lobes in the vorticity field, which reduce the zonal fetch of the total vorticity perturbation when the superposition of all the evolved basin modes is considered, and the resulting perturbation more closely resembles [Figs. 8g, 8h](#), [5i](#), and [5j](#).

The role of short Rossby waves in controlling the stochastically induced variability is further illustrated in [Fig. 9m](#), which shows a perturbation with an initial structure identical to \mathbf{S}_1 after it has evolved for 15 days in a resting ocean. The emergence of the short Rossby wave components along the western boundary, due to linear interference of the nonorthogonal basin modes, is evident. In the presence of the two-gyre circulation, it is these short Rossby waves that interact with the basic state flow as demonstrated above and generate the perturbation patterns like those shown in [Fig. 5i](#).

The above analysis concentrates on the perturbation enstrophy dynamics of stochastically induced perturbations. The perturbation energy dynamics are more straight forward and can be understood in terms of the orientation of the plane parallel Rossby wave phase lines relative to the basic-state flow. Energy growth (decay) is expected where Rossby wave phase lines tilt upstream (downstream) relative to the basic state flow.

5. Nonautonomous systems

So far, our attention has been confined to autonomous systems where \mathbf{A} described by (5) is independent of time. However, many problems of interest are nonautonomous, and this will be the subject of this section.

Consider now the nonautonomous system:

$$\frac{d\mathbf{z}}{dt} = \mathbf{A}(t)\mathbf{z}. \quad (16)$$

Unlike the autonomous case, the eigenmodes of $\mathbf{A}(t)$ no longer characterise the properties of the system for all time because the basic state is continually changing.

a. Singular vectors and Lyapunov vectors

The stability of nonautonomous systems has traditionally been examined in terms of Lyapunov exponents (Lyapunov 1907). The Lyapunov exponents κ_i can be defined as

$$\kappa_i = \lim_{t_2 \rightarrow \infty} \frac{1}{(t_2 - t_1)} \ln \left\{ \frac{\|\mathbf{R}(t_1, t_2)\mathbf{g}_i\|}{\|\mathbf{g}_i\|} \right\}, \quad (17)$$

where $\mathbf{R}(t_1, t_2)$ is the propagator of (16) over the time interval $t = [t_1, t_2]$, and \mathbf{g}_i are the associated Lyapunov vectors. If (16) represents the linearization of a nonlinear system, then the significance of the Lyapunov exponents κ_i is that nearby trajectories of the system initially separated by an infinitesimal distance in the direction of \mathbf{g}_i will separate at a rate of $e^{\kappa_i t}$. Therefore a positive Lyapunov exponent indicates an exponential loss of correlation between two trajectories of the system starting at neighbouring points. Since the initial trajectories are separated by an infinitesimal distance, the linear equation (16) is assumed to be valid at all times.

The Lyapunov exponents and the singular values of $\mathbf{R}(t_1, t_2)$ are in fact related. Following Goldhirsch et al. (1987), the eigenvalues of $\mathbf{R}^T(0, t)\mathbf{R}(0, t)$ can be expressed as $e^{v_i(t)t}$, and it can be shown that

$$v_i(t) = \kappa_i + (b_i + \xi_i(t))/t, \quad (18)$$

where the b_i are constants and $\xi_i(t)$ are noise terms. Thus as $t \rightarrow \infty$, $v_i(t) \rightarrow \kappa_i$, and the singular vectors become the optimal excitations for the Lyapunov vectors \mathbf{g}_i .

To illustrate the connection between the singular values and Lyapunov exponents, we will use the double-gyre ocean circulation described by (1) in the rectangular ocean basin subject to a steady wind forcing as in section 3. The Lyapunov exponent computations described below are computationally very demanding for the high-resolution model since optimal growth times of several thousand days are required to reliably estimate the Lyapunov exponents (see appendix B). For this reason the low-resolution model was used in the experiments reported here. Computations reveal that the results of sections 3 and 4 are qualitatively similar for both the high and low resolution versions of the model, and both yield identical conclusions about the importance of non-normality for controlling perturbation growth in the ocean.² The same will be true for the related experiments presented in this section, so our use of the low-resolution model here is justified.

In the present case the strength of the wind forcing was increased by 50% over that used in appendix A, corresponding to a surface Ekman pumping amplitude of $6.465 \times 10^{-6} \text{ m s}^{-1}$. This yields a double-gyre circulation that is time dependent and characterized by transient eddy activity. Figure 10 shows time series of basin integrated energy ($-\Pi^T \Psi$) and enstrophy ($\Pi^T \Pi$) from a 30 000 day integration of the model started from a state of rest. Figure 11 shows snapshots of the stream function 1000 days apart during the last 5000 days of integration.

Figure 12 shows $v_1(t)$ as a function of the inverse of the growth time t for the vorticity equation linearized about the time evolving circulation shown in Figs. 10 and 11. According to (18), $v_1(t)$ varies approximately linearly with $1/t$ which is confirmed in Fig. 12. By performing a least squares best fit of the points in Fig. 12 to a straight line we can estimate κ_1 (the first Lyapunov exponent of the system) as the intercept of the straight line with the v_1 axis. Table 1 shows various estimates of κ_1 obtained in this way using different portions of the time-evolving trajectory shown in Figs. 10 and 11. All of these calculations suggest that $\kappa_1 > 0$. Similar results were obtained if the perturbation energy norm was used instead of the perturbation enstrophy norm.

Figure 13a shows the initial vorticity structure of our estimate of the first Lyapunov vector \mathbf{g}_1 . A timeseries of Q for the time-evolving Lyapunov vector is shown in Fig. 13b. Note that in Fig. 13b the exponential growth factor associated with κ_1 has been suppressed. Figure 13b indicates that the Lyapunov vector is characterized by oscillations of several different frequencies, the lowest frequency having a period of ~ 5800 days. Figures 13c-f show snapshots of

streamfunction separated by approximately 1/4 of this period. The Lyapunov vector is similar to anomalies found by [Chang et al. \(2001; Fig. 11\)](#) propagating in an unstable double gyre circulation using a higher-resolution model than that used here, but in a similar dynamical regime.

b. Non-normality and Lyapunov vectors

In a recent study, [Farrell and Ioannou \(1999\)](#), hereafter FI99 consider the role played by non-normality in shaping the Lyapunov vectors of nonautonomous systems. Following [Farrell and Ioannou \(1996b\)](#), FI99 express the time-dependent operator in (16) as $\mathbf{A}(t) = \bar{\mathbf{A}} + \mathbf{A}'(t)$ where $\bar{\mathbf{A}}$ represents the time mean of $\mathbf{A}(t)$. The system (16) can then be viewed as an autonomous system governed by $\bar{\mathbf{A}}$ subject to a multiplicative forcing $\mathbf{A}'(t)$. FI99 show that if $\bar{\mathbf{A}}$ and $\mathbf{A}'(t)$ do not commute, and if $\mathbf{A}'(t)$ mixes at least two eigenmodes of $\bar{\mathbf{A}}$ then the system will be non-normal. Therefore, except in very special cases, nonautonomous systems are non-normal.

FI99 considered several examples of nonautonomous systems in which $\mathbf{A}'(t)$ was treated as a red noise process. Of particular interest is the degree of non-normality of $\bar{\mathbf{A}}$. FI99 considered the projection of the first Lyapunov vector of (16) on the eigenmodes of $\bar{\mathbf{A}}$ and found that the most non-normal eigenmodes are favoured by the Lyapunov vector. It is of interest to see if these ideas carry over to the time dependent wind-driven ocean circulation shown in [Figs. 10](#) and [11](#). Small perturbations to the circulation are governed by the tangent linear equation (2) where Ψ and Π are time dependent. In this case we have $\mathbf{A} \equiv -aJ(\Psi, \cdot) - aJ(\nabla^2 \cdot, \Pi) - \partial \nabla^2 \cdot / \partial x - \gamma \cdot$ and $\mathbf{A}'(t) \equiv -aJ(\Psi', \cdot) - aJ(\nabla^2 \cdot, \Pi')$ where $\Psi(t) = \bar{\Psi} + \Psi'(t)$, $\Pi(t) = \bar{\Pi} + \Pi'(t)$ and an overbar denotes the time mean. [Figure 14a](#) shows $\bar{\Psi}$ averaged between days 10 000 and 30 000 in [Fig. 10](#). [Figure 14b](#) shows the measure of non-normality $|v_k|$ vs σ_i for the subset of eigenmodes Λ_c of $\bar{\mathbf{A}}$ (see [section 3a](#)) computed from [Fig. 14a](#), where σ_i is the imaginary component of the eigenfrequency. The most non-normal, least-damped eigenmodes generally have low frequencies. If we denote the Lyapunov vector at anytime as $\mathbf{g}_1 = \sum_k a_k \hat{\mathbf{S}}_k$ where $\hat{\mathbf{S}}_k$ are the eigenmodes of $\bar{\mathbf{A}}$, the projection $|a_k|$ of the perturbation in [Fig. 13a](#) on each eigenmode in [Fig. 14b](#) is shown in [Fig. 14c](#). Clearly, the eigenmodes on which the Lyapunov vector has the largest projection are some of the most non-normal, least-damped, low-frequency eigenmodes, a result that is in general agreement with FI99. This is generally true at other times also as illustrated in [Figs. 14d–g](#), which show the projection of \mathbf{g}_1 on the eigenmodes of $\bar{\mathbf{A}}$ at the times corresponding to [Figs. 13c–f](#).

6. Summary and discussion

In this paper we have applied the ideas of generalized linear stability theory to the familiar wind-driven double-gyre ocean circulation described by the quasigeostrophic barotropic vorticity equation. The development of perturbations on the flow was first explored using the tangent linear equation linearized about a steady, asymptotically stable circulation. The non-normal character of the wind-driven circulation due to the straining components of the flow was quantified by computing the norm of the resolvent matrix and by calculating the degree of linear dependence of the system eigenmodes. As a result of non-normality, transient growth of both perturbation energy E and perturbation enstrophy Q was found to be possible over a wide range of time intervals, where E and Q are liberated from the basic-state flow by perturbations via barotropic processes. This can also be viewed geometrically as the linear interference of the nonorthogonal eigenmodes.

Stochastic wind stress forcing represents a continual source of perturbations for the ocean circulation, and non-normality implies that stochastically induced variability may be significantly enhanced by the transient growth of such perturbations. The dynamics of stochastically induced variability was explored in terms of the system eigenmodes, and an interesting physical mechanism for maintaining variance was discussed involving primarily short Rossby wave dynamics. The short Rossby waves undergo transient growth in the western boundary current regions since it is here that the straining components of the circulation are largest and where E_R and Q_R in (3) and (4) dominate the perturbation energy and enstrophy dynamics. The transient growth of short Rossby waves near the western boundary is manifested as growing small scale disturbances along the western boundary current and its offshore extension. Thus in response to the basin-scale components of the stochastic Ekman pumping there is an apparent reduction in scale of the ocean response in the western boundary current region. Potential sources of stochastic, large-scale Ekman pumping anomalies in nature are the atmospheric teleconnection patterns such as the Pacific North American pattern or North Atlantic oscillation. The observed amplitudes of the teleconnection patterns undergo significant stochastic variations in time. The dominant stochastic optimal \mathbf{S}_1 and the least-damped adjoint eigenmode ([Fig. 7b](#)) onto which \mathbf{S}_1 projects are qualitatively similar to the pattern of Ekman pumping observed in connection with the North Atlantic oscillation (see [Fig. 1b](#) of [Marshall et al. 2001](#)).

Many eddy resolving models of the ocean circulation tend to underestimate the eddy energy of the ocean. It has been postulated that this deficiency may be due to the stochastic or high frequency components of the surface forcing that are typically not well resolved by traditional observing systems and have not been included in model simulations. The results of the present study suggest a potential mechanism by which stochastic variations of the teleconnection pattern amplitudes may enhance eddy kinetic energy in the western boundary current regions. The results of some modeling studies (e.g., [Fu and Smith 1996](#)) certainly do suggest that intraseasonal variations in the surface wind stress can enhance the variability of ocean western boundary currents.

The nature of non-normal systems may require us to view the ocean circulation in a different light. Most published studies of observed meander growth and eddy formation in the ocean have adopted the view that these features are due to an inherent hydrodynamic instability in the system that can be explained using the traditional notion of barotropic and baroclinic instability. However, the experiments of sections 4 reveal that stochastic forcing can excite meanders and eddies in the

ocean in the form of transient events that are not associated with flow that is unstable in the traditional sense. It may be very difficult, if not impossible, to distinguish between a meander or eddy that was stochastically forced and undergoing transient development as opposed to one that is developing on an inherently unstable flow. However this distinction is clearly important for the interpretation of observations and has important implications for ocean prediction. Eddy-resolving simulations of the ocean reveal that the ocean is most likely intrinsically unstable over most of the globe. So, depending on the local character of the flow in which they develop, stochastically induced perturbations may undergo transient growth, or grow via the dynamics of an unstable eigenmode. Thus, the eddy dynamics and statistics of the resulting eddy field and circulation will most likely depend on the interplay between non-normal transient growth and the growth of unstable modes.

The response of the ocean to stochastic forcing has been the subject of many previous studies. It is therefore of interest to discuss the relevance of the approach adopted here in the light of previous results. For the barotropic component of the circulation, various studies reviewed by [Moore \(1999\)](#) suggest the following. For “low” frequency stochastic forcing [<0.01 cycles per day (cpd)] the ocean response is primarily given by a local Sverdrup balance. For “intermediate” frequency stochastic forcing (~ 0.01 – 0.1 cpd) the ocean response is primarily in the form of barotropic Rossby waves. For “high” frequency stochastic forcing (>0.1 cpd) there is thought to be no appreciable ocean response. Since previous studies suggest that there is a well defined cutoff in the ocean response to “high” frequency forcing, we will discuss this last point further. This argument, however, is based on the traditional notion of resonance applied to barotropic Rossby waves in an infinite resting ocean, or Rossby waves in a resting bounded rectangular ocean with the dimensions of the North Atlantic. However the results of the present study suggest something different.

The eigenfrequencies of the resting ocean basin modes in the high-resolution model are shown in [Fig. 15](#). A comparison of these with the subset Λ_c (see [section 3a](#)) of the eigen-spectrum of the double-gyre circulation of the high resolution model shown in [Fig. 2a](#) reveals that the presence of a mean flow shifts the eigenmodes to higher frequencies. The frequency cutoff at 0.1 cpd cited in the previous literature corresponds to the highest frequency basin mode in a resting rectangular ocean with the dimensions of the North Atlantic. The basin mode frequencies depend on the dimensions of the basin, and in the present study, the ocean basin measures 1000×2000 km, which is somewhat smaller than the North Atlantic. Thus the maximum basin mode frequency of our ocean basin (~ 0.04 cpd) is less than that of a basin the size of the North Atlantic so please bear this in mind in the following discussion. In the present study, the highest frequency basin mode for the resting ocean has a period of 25.58 days. In the presence of the double gyre circulation, [Fig. 15](#) shows that the highest-frequency eigenmode of the subset Λ_c has a period of 2.7 days. Thus the mean wind-driven circulation has effectively decreased the period of the highest-frequency eigenmode by an order of magnitude compared to a resting ocean. If the eigenmode frequencies in a basin the size of the North Atlantic are shifted in the same way by the presence of the subtropical and subpolar gyres, then we might anticipate a significant increase in the cutoff frequency of the ocean response compared to that suggested by the basin mode frequencies.

In the high-resolution model, each basin mode is damped at the same rate [$\sim (14.5 \text{ day})^{-1}$]. [Figure 2a](#) reveals that the highest-frequency eigenmodes of the double-gyre circulation are damped much faster than this. Based on the usual ideas of resonance, one might anticipate that the response of the double-gyre circulation at forcing periods of less than 25 days or so would be small because of the rapid damping time of the associated eigenmodes with shorter periods. Recall, however, that $\|\mathcal{R}(\omega)\|$ provides an upper bound on the ratio of the response to the size of the forcing at the forcing frequency ω . [Figure 15](#) shows a plot of $\log_{10} \|\mathcal{R}(\omega)\|$ vs ω for purely oscillatory forcing (i.e., $\omega_r = 0$), and suggests that by virtue of non-normality, the ocean response to forcing frequencies in excess of 0.04 cpd (the basin mode cutoff frequency in our ocean model) can be potentially amplified by more than an order of magnitude. The classical resonance arguments invoked in previous studies assume that the resonant basin mode response varies as $1/\text{dist}(\omega, \Lambda)$ where Λ represents the spectrum of basin mode frequencies. For comparison, $\log_{10}[1/\text{dist}(\omega, \Lambda)]$ versus ω is shown in [Fig. 15](#) for the basin modes of the resting ocean confirming the rapid drop in response for $\omega > 0.04$ cpd, the highest basin model frequency in our ocean basin. [Figure 15](#) shows that the response of the double gyre circulation due to non-normality may be significantly larger at all frequencies than that anticipated from classical resonance arguments. This amplification effect is sometimes referred to as pseudo-resonance ([Trefethen et al. 1993](#)), and is a direct consequence of the non-normality of the system and the sources of variance introduced by linear eigenmode interference.

Recall that the adjoint eigenmodes are the optimal excitations of the corresponding eigenmodes. A comparison of the adjoint eigenmodes of the resting ocean and those of the double gyre circulation reveals an interesting difference between the two systems with regard to the scale of the response relative to the scale of the forcing. The basin modes are the eigenmodes of (2) for $\alpha = 0$. It is easy to show that for the Q norm, the vorticity structure of an adjoint basin mode is identical to the streamfunction of the corresponding basin mode. The basin mode with highest frequency in [Fig. 15](#) is the eigenmode with the largest horizontal scale (cf. [Fig. 9e](#)). The corresponding adjoint basin mode is therefore also large scale. Conversely, the lowest frequency basin modes and adjoint basin modes have the smallest scales. Therefore in a resting ocean, large- (small) scale forcing excites high- (low) frequency, large- (small) scale basin modes. In the double gyre ocean, the situation can be quite different due to the presence of other, non-normal eigenmodes. The least damped eigenmode of [Fig. 7](#) is a graphic example of this, and illustrates how a small-scale, low-frequency response ([Fig. 7a](#)) can be generated by a relatively large-scale, low-frequency forcing ([Fig. 7b](#)). We should note that eigenmodes resembling some of the high frequency basin modes are supported by the double-gyre circulation also so large scale, high frequency forcing can excite a like response, just as in a resting ocean. However, [Figs. 5g–j](#) suggest that this may not be the dominant process occurring due to the high degree of linear dependence of eigenmodes like that in [Fig. 7](#) on the other members of the eigenspectrum.

The results of this study shed new light on the response of the wind-driven ocean circulation to stochastic forcing. The straining components of the circulation play several important roles in controlling the ocean response: (i) they shift the

eigenspectra of the system to higher frequencies; (ii) they increase the non-normality of the system by increasing the linear dependence of the eigenmodes, thus enhancing the pseudoresonant response of the system at all frequencies; and (iii) they fundamentally change the relationship between the scale of the forcing and the scale of the subsequent response within different frequency ranges. The combined result of all these effects is that the ocean will most likely respond to stochastic variations in surface wind stress over a wider band of frequencies and space scales than previous studies have suggested. The results of [section 5](#) suggest that these ideas may also prove useful for understanding the dynamics of unstable circulations.

Acknowledgments

This work was supported by grants from the NSF Physical Oceanography and Climate Dynamics Programs (OCE-9696199, ATM9809790, and OCE-0002370). Discussions with Profs. Brian Farrell and Jeff Weiss are gratefully acknowledged. We are grateful to Prof. Dan Sorensen for making the ARPACK library freely available. We are also grateful to the reviewers for their very insightful comments on earlier versions of the manuscript.

REFERENCES

- Blumenthal M. B., 1991: Predictability of a coupled ocean–atmosphere model. *J. Climate*, **4**, 766–784. [Find this article online](#)
- Borges M. D., and D. L. Hartmann, 1992: Barotropic instability and optimal perturbations of observed nonzonal flows. *J. Atmos. Sci.*, **49**, 335–354. [Find this article online](#)
- Boyd J. P., 1983: The continuous spectrum of linear Couette flow with the beta effect. *J. Atmos. Sci.*, **40**, 2304–2308. [Find this article online](#)
- Branstator G., 1985: Analysis of general circulation model sea-surface temperature anomaly simulations using a linear model. Part II: Eigenanalysis. *J. Atmos. Sci.*, **42**, 2242–2254. [Find this article online](#)
- Buizza R., 1995: Optimal perturbation time evolution and sensitivity of ensemble prediction to perturbation amplitude. *Quart. J. Roy. Meteor. Soc.*, **121**, 1705–1738. [Find this article online](#)
- Buizza R., 1997: Potential forecast skill of ensemble prediction and spread and skill distributions of the ECMWF ensemble prediction system. *Mon. Wea. Rev.*, **125**, 99–119. [Find this article online](#)
- Buizza R., and T. N. Palmer, 1995: The singular-vector structure of the atmospheric global circulation. *J. Atmos. Sci.*, **52**, 1434–1456. [Find this article online](#)
- Buizza R., J. Tribbia, F. Molteni, and T. Palmer, 1993: Computation of optimal unstable structures for a numerical weather prediction model. *Tellus*, **45A**, 388–407. [Find this article online](#)
- Butler K. M., and B. F. Farrell, 1992: Three dimensional optimal perturbations in viscous shear flow. *Phys. Fluids A*, **4**, 1637–1650. [Find this article online](#)
- Chang K.-I., M. Ghil, K. Ide, and C.-C. Lai, 2001: Transitions to aperiodic variability in a wind-driven double-gyre circulation model. *J. Phys. Oceanogr.*, **31**, 1260–1286. [Find this article online](#)
- Chave A. S., D. S. Luther, and J. H. Filloux, 1991: Variability of the wind stress curl over the North Pacific: Implications for the oceanic response. *J. Geophys. Res.*, **96**, 18661–18379. [Find this article online](#)
- Chen Y.-Q., D. S. Battisti, T. N. Palmer, J. Barsugli, and E. S. Sarachik, 1997: A study of the predictability of tropical Pacific SST in a coupled atmosphere–ocean model using singular vector analysis: The role of the annual cycle and the ENSO cycle. *Mon. Wea. Rev.*, **125**, 831–845. [Find this article online](#)
- DelSole T. M., 1996: Can quasigeostrophic turbulence be modeled stochastically? *J. Atmos. Sci.*, **53**, 1617–1633. [Find this article online](#)
- DelSole T. M., 1999: Stochastic models of shear-flow turbulence with enstrophy transfer to subgrid scales. *J. Atmos. Sci.*, **56**, 3692–3703. [Find this article online](#)
- DelSole T. M., and B. F. Farrell, 1994: Nonlinear equilibration of localized instabilities on a baroclinic jet. *J. Atmos. Sci.*, **51**, 2270–2284. [Find this article online](#)
- DelSole T. M., 1995: A stochastically excited linear system as a model for quasigeostrophic turbulence: Analytic results for one- and two-layer fluids. *J. Atmos. Sci.*, **52**, 2531–2547. [Find this article online](#)
- DelSole T. M., and A. Y. Hou, 1999: Empirical stochastic models for the dominant climate statistics of a general circulation model. *Mon. Wea. Rev.*, **127**, 2533–2545. [Find this article online](#)
- Eckert C., 1999: On predictability limits of ENSO. A study performed with a simplified model of the tropical pacific ocean-atmosphere system. Examensarbeit Nr. 55, 76 pp. [Available from: Max Planck Institut fuer Meteorologie, Bundesstrasse 55 D-20146, Hamburg, Germany.].

Ehrendorfer M., and J. J. Tribbia, 1997: Optimal prediction of forecast error covariances through singular vectors. *J. Atmos. Sci.*, **54**, 286–313. [Find this article online](#)

Errico R. M., T. Vukicic, and K. Raeder, 1993: Examination of the accuracy of a tangent linear model. *Tellus*, **45A**, 462–477. [Find this article online](#)

Fan Y., 1998: ENSO prediction and predictability in an intermediate coupled model. Ph.D. thesis, University of Oxford, 241 pp.

Fan Y., M. R. Allen, D. L. T. Anderson, and M. A. Balmaseda, 2000: How predictability depends on the nature of uncertainty in initial conditions in a coupled model of ENSO. *J. Climate*, **13**, 3298–3313. [Find this article online](#)

Farrell B. F., 1982a: The initial growth of disturbances in baroclinic flow. *J. Atmos. Sci.*, **39**, 1663–1686. [Find this article online](#)

Farrell B. F., 1982b: Pulse asymptotics of the Charney baroclinic instability problem. *J. Atmos. Sci.*, **39**, 507–517. [Find this article online](#)

Farrell B. F., 1984: Modal and nonmodal baroclinic waves. *J. Atmos. Sci.*, **41**, 668–673. [Find this article online](#)

Farrell B. F., 1985: Transient growth of damped baroclinic waves. *J. Atmos. Sci.*, **42**, 2718–2727. [Find this article online](#)

Farrell B. F., 1988a: Optimal excitation of neutral Rossby waves. *J. Atmos. Sci.*, **45**, 163–172. [Find this article online](#)

Farrell B. F., 1988b: Optimal excitation of perturbations in viscous shear flow. *Phys. Fluids*, **31**, 2093–2102. [Find this article online](#)

Farrell B. F., 1989a: Optimal excitation of baroclinic waves. *J. Atmos. Sci.*, **46**, 1193–1206. [Find this article online](#)

Farrell B. F., 1989b: Transient development in confluent and diffluent flow. *J. Atmos. Sci.*, **46**, 3279–3288. [Find this article online](#)

Farrell B. F., 1990: Small error dynamics and the predictability of atmospheric flows. *J. Atmos. Sci.*, **47**, 2409–2416. [Find this article online](#)

Farrell B. F., and A. M. Moore, 1992: An adjoint method for obtaining the most rapidly growing perturbation to oceanic flows. *J. Phys. Oceanogr.*, **22**, 338–349. [Find this article online](#)

Farrell B. F., and P. J. Ioannou, 1993a: Optimal excitation of three dimensional perturbations in viscous constant shear flow. *Phys. Fluids A*, **5**, 1390–1400. [Find this article online](#)

Farrell B. F., 1993b: Perturbation growth in shear flow exhibits universality. *Phys. Fluids A*, **5**, 2298–2300. [Find this article online](#)

Farrell B. F., 1993c: Transient development of perturbations in stratified shear flow. *J. Atmos. Sci.*, **50**, 2201–2214. [Find this article online](#)

Farrell B. F., 1993d: Stochastic dynamics of baroclinic waves. *J. Atmos. Sci.*, **50**, 4044–4057. [Find this article online](#)

Farrell B. F., 1993e: Stochastic forcing of the linearized Navier–Stokes equations. *Phys. Fluids A*, **5**, 2600–2609. [Find this article online](#)

Farrell B. F., 1993f: Stochastic forcing of perturbation variance in unbounded shear and deformation flows. *J. Atmos. Sci.*, **50**, 200–211. [Find this article online](#)

Farrell B. F., 1994a: A theory for the statistical equilibrium energy spectrum and heat flux produced by transient baroclinic waves. *J. Atmos. Sci.*, **51**, 2685–2698. [Find this article online](#)

Farrell B. F., 1994b: Variance maintained by stochastic forcing of nonnormal dynamical systems associated with linearly stable shear flows. *Phys. Rev. Lett.*, **72**, 1188–1191. [Find this article online](#)

Farrell B. F., 1996a: Generalized stability theory. Part I: Autonomous operators. *J. Atmos. Sci.*, **53**, 2025–2040. [Find this article online](#)

Farrell B. F., 1996b: Generalized stability theory. Part II: Nonautonomous operators. *J. Atmos. Sci.*, **53**, 2041–2053. [Find this article online](#)

Farrell B. F., 1996c: Turbulence suppression by active control. *Phys. Fluids A*, **8**, 1257–1268. [Find this article online](#)

Farrell B. F., 1999: Perturbation growth and structure in time dependent flows. *J. Atmos. Sci.*, **56**, 3622–3639. [Find this article online](#)

Ferranti L., T. N. Palmer, F. Molteni, and E. Klinker, 1990: Tropical–extratropical interaction with the 30–60 day oscillation and its impact on medium and extended range prediction. *J. Atmos. Sci.*, **47**, 2177–2199. [Find this article online](#)

Fu L.-L., and R. D. Smith, 1996: Global ocean circulation from satellite altimetry and high-resolution computer simulation. *Bull. Amer. Meteor. Soc.*, **77**, 2625–2636. [Find this article online](#)

Goldhirsch I., P.-L. Sulem, and S. A. Orzag, 1987: Stability and Lyapunov stability of dynamical systems: A differential approach and numerical method. *Physica D*, **27**, 311–337. [Find this article online](#)

Golub G. H., and C. F. van Loan, 1989: *Matrix Computations*. Johns Hopkins University Press, 642 pp.

Haidvogel D. B., A. R. Robinson, and E. E. Schulman, 1980: The accuracy, efficiency and stability of three numerical models with application to open ocean problems. *J. Comput. Phys.*, **34**, 1–53. [Find this article online](#)

Hartmann D. L., R. Buizza, and T. N. Palmer, 1995: Singular vectors: the effect of spatial scale on linear growth of disturbances. *J. Atmos. Sci.*, **52**, 3885–3894. [Find this article online](#)

Hellerman S., and M. Rosenstein, 1983: Normal monthly windstress over the world ocean with error estimates. *J. Phys. Oceanogr.*, **13**, 1093–1104. [Find this article online](#)

Ioannou P. J., 1995: Nonnormality increases variance. *J. Atmos. Sci.*, **52**, 1155–1158. [Find this article online](#)

Johnson S., 1999: Markov model studies of the El Niño Southern Oscillation. Ph.D. Thesis, University of Washington, 143 pp.

Joly A., 1995: The stability of steady fronts and the adjoint method: Nonmodal frontal waves. *J. Atmos. Sci.*, **52**, 3082–3108. [Find this article online](#)

Kelvin, 1887: Stability of fluid motions: Rectilinear motion of a viscous fluid between two parallel plate. *Philos. Mag.*, **24**, 188–196. [Find this article online](#)

Kleeman R., and A. M. Moore, 1997: A theory for the limitations of ENSO predictability due to stochastic atmospheric transients. *J. Atmos. Sci.*, **54**, 753–767. [Find this article online](#)

Kleeman R., 1999: A new method for determining the reliability of dynamical ENSO predictions. *Mon. Wea. Rev.*, **127**, 694–705. [Find this article online](#)

Lacarra J.-F., and O. Talagrand, 1988: Short-range evolution of small perturbations in a barotropic model. *Tellus*, **40A**, 81–95. [Find this article online](#)

Lehoucq R. B., D. C. Sorensen, and C. Yang, 1997: ARPACK users' guide: Solution of large scale eigenvalue problems with implicitly restarted Arnoldi methods. Rice University, 140 pp.

Lorenz E. N., 1965: A study of the predictability of a 28-variable atmospheric model. *Tellus*, **17**, 321–333. [Find this article online](#)

Lyapunov A. M., 1907: Probleme general de la stabilite du mouvement. *Ann. Fac. Sci. Univ. Toulouse*, **9**, 203–475. [Find this article online](#)

Mak M., and M. Cai, 1989: Local barotropic instability. *J. Atmos. Sci.*, **46**, 3289–3311. [Find this article online](#)

Marshall J. C., 1984: Eddy-mean-flow interaction in a barotropic ocean model. *Quart. J. Roy. Meteor. Soc.*, **110**, 573–590. [Find this article online](#)

Marshall J. C., H. Johnson, and J. Goodman, 2001: A study of the interaction of the North Atlantic oscillation with ocean circulation. *J. Climate*, **14**, 1399–1421. [Find this article online](#)

Miller R. N., A. R. Robinson, and D. B. Haidvogel, 1981: A baroclinic quasi-geostrophic open ocean model. *J. Comput. Phys.*, **50**, 38–70. [Find this article online](#)

Molteni F., R. Mureau, and T. N. Palmer, 1993: Predictability and finite time instability of the northern winter circulation. *Quart. J. Roy. Meteor. Soc.*, **119**, 269–298. [Find this article online](#)

Molteni F., R. Buizza, T. N. Palmer, and T. Petroligis, 1996: The ECMWF ensemble prediction system: Methodology and validation. *Quart. J. Roy. Meteor. Soc.*, **122**, 73–120. [Find this article online](#)

Moore A. M., 1991: Data assimilation in a quasigeostrophic open ocean model of the Gulf Stream region using the adjoint method. *J. Phys. Oceanogr.*, **21**, 398–427. [Find this article online](#)

Moore A. M., 1999: Wind-induced variability of ocean gyres. *Dyn. Atmos. Oceans*, **29**, 335–364. [Find this article online](#)

Moore A. M., and B. F. Farrell, 1993: Rapid perturbation growth on spatially and temporally varying oceanic flows determined using an adjoint method: Application to the Gulf Stream. *J. Phys. Oceanogr.*, **23**, 1682–1702. [Find this article online](#)

Moore A. M., and R. Kleeman, 1996: The dynamics of error growth and predictability in a coupled model of ENSO. *Quart. J. Roy. Meteor. Soc.*, **122**, 1405–1446. [Find this article online](#)

Moore A. M., 1997a: The singular vectors of a coupled ocean-atmosphere model of ENSO. Part I: Thermodynamics, energetics and error growth. *Quart. J. Roy. Meteor. Soc.*, **123**, 953–981. [Find this article online](#)

Moore A. M., 1997b: The singular vectors of a coupled ocean-atmosphere model of ENSO. Part II: Sensitivity studies and dynamical significance. *Quart. J. Roy. Meteor. Soc.*, **123**, 983–1006. [Find this article online](#)

Moore A. M., 1998: Skill assessment for ENSO using ensemble prediction. *Quart. J. Roy. Meteor. Soc.*, **124**, 557–584. [Find this article online](#)

Moore A. M., 1999a: The nonnormal nature of El Niño and intraseasonal variability. *J. Climate*, **12**, 2965–2982. [Find this article online](#)

Moore A. M., 1999b: Stochastic forcing of ENSO by the intraseasonal oscillation. *J. Climate*, **12**, 1199–1220. [Find this article online](#)

Moore A. M., 2001: The differences between the optimal perturbations of coupled models of ENSO. *J. Climate*, **14**, 138–163. [Find this article online](#)

Mureau R., F. Molteni, and T. N. Palmer, 1993: Ensemble prediction using dynamically conditioned perturbations. *Quart. J. Roy. Meteor. Soc.*, **119**, 299–323. [Find this article online](#)

Palmer T. N., 1996: Predictability of the atmosphere and oceans: From days to decades. *Decadal Climate Variability: Dynamics and Predictability*, D. L. T. Anderson and J. Willebrand, Eds., Springer, 83–155.

Pedlosky J., 1965: A note on the western intensification of the oceanic circulation. *J. Mar. Res.*, **23**, 207. [Find this article online](#)

Pedlosky J., 1979: *Geophysical Fluid Dynamics*. Springer-Verlag, 710 pp.

Pedlosky J., 1996: *Ocean Circulation Theory*. Springer-Verlag, 453 pp.

Penland C., 1989: Random forcing and forecasting using principal oscillation pattern analysis. *Mon. Wea. Rev.*, **117**, 2165–2185. [Find this article online](#)

Penland C., 1996: A stochastic model of IndoPacific sea surface temperature anomalies. *Physica D*, **98**, 534–558. [Find this article online](#)

Penland C., and P. D. Sardeshmukh, 1995a: Error and sensitivity analysis of geophysical eigensystems. *J. Climate*, **8**, 1988–1998. [Find this article online](#)

Penland C., 1995b: The optimal growth of tropical sea surface temperature anomalies. *J. Climate*, **8**, 1999–2024. [Find this article online](#)

Press W. H., B. P. Flannery, S. A. Teukolsky, and W. T. Vetterling, 1986: *Numerical Recipes*. Cambridge University Press, 702 pp.

Rayleigh J. W. S., 1880: On the stability or instability of certain fluid motions. *Proc. London Math. Soc.*, **9**, 57–70. [Find this article online](#)

Reddy S. C., P. J. Schmid, and D. S. Henningson, 1993: Pseudospectra of the Orr–Sommerfeld operator. *SIAM J. Appl. Math.*, **53**, 15–47. [Find this article online](#)

Rhines P. B., 1977: The dynamics of insteady currents. *The Sea*, E. D. Goldberg et al., Eds., Vol. 6, Wiley and Sons, 189–318.

Samelson R. M., and B. Shroyer, 1991: Currents forced by stochastic winds with meridionally varying amplitude. *J. Geophys. Res.*, **96**, 18425–18429. [Find this article online](#)

Shapiro R., 1970: Smoothing, filtering and boundary effects. *Rev. Geophys. Space Phys.*, **8**, 359–386. [Find this article online](#)

Sura P., F. Lunkeit, and K. Fraedrich, 2000: Decadal variability in a simplified wind-driven ocean model. *J. Phys. Oceanogr.*, **30**, 1917–1930. [Find this article online](#)

Thompson C. J., 1998: Initial conditions for optimal growth in a coupled ocean–atmosphere model of ENSO. *J. Atmos. Sci.*, **55**, 537–557. [Find this article online](#)

Trefethen L. N., 1996: Pseudospectra of linear operators. *SIAM Rev.*, **39**, 383–406. [Find this article online](#)

Trefethen L. N., A. E. Trefethen, S. C. Reddy, and T. A. Driscoll, 1993: Hydrodynamic stability without eigenvalues. *Science*, **261**, 578–584. [Find this article online](#)

Willebrand J., 1978: Temporal and spatial scales of the wind field over the North Pacific and North Atlantic. *J. Phys. Oceanogr.*, **8**, 1080–1094. [Find this article online](#)

Xue Y., M. A. Cane, S. E. Zebiak, and M. B. Blumenthal, 1994: On the prediction of ENSO: A study with a low order Markov model. *Tellus*, **46A**, 512–528. [Find this article online](#)

Xue Y., 1997a: Predictability of a coupled model of ENSO using singular vector analysis. Part I: Optimal growth in seasonal background and ENSO cycles. *Mon. Wea. Rev.*, **125**, 2043–2056. [Find this article online](#)

Xue Y., and T. N. Palmer, 1997b: Predictability of a coupled model of ENSO using singular vector analysis. Part II: Optimal growth and forecast skill. *Mon. Wea. Rev.*, **125**, 2057–2073. [Find this article online](#)

Xue Y., A. Leetmaa, and M. Ji, 1999: Impact of sea level on predictability of ENSO: A study with Markov model. *Second Hayes Symp. on Seasonal to Int. Climate Variability—The 1997/1998 ENSO Cycle*, Dallas, TX, Amer. Meteor. Soc. 81–84.

Zeng Q.-C., 1983: The evolution of a Rossby-wave packet in a three-dimensional baroclinic atmosphere. *J. Atmos. Sci.*, **40**, 73–89. [Find this article online](#)

Zhang Z., 1988: The linear study if zonally asymmetric barotropic flows. Ph.D. Thesis, University of Reading.

Zou X., A. Barcilon, I. M. Navon, J. Whitaker, and D. G. Cacuci, 1993: An adjoint sensitivity study of blocking in a two-layer isentropic model. *Mon. Wea. Rev.*, **121**, 2833–2857. [Find this article online](#)

7. The Quasigeostrophic Ocean Model

The ideas described in this paper have been applied to the wind-forced, quasigeostrophic, barotropic vorticity equation on a middle-latitude β -plane. The vorticity equation is nondimensionalized by scaling velocity by U , horizontal distance by d , depth by H , streamfunction Ψ by Ud , and time by $(\beta d)^{-1}$ where β is the meridional gradient of the Coriolis parameter. The nondimensional vorticity equation can be written as

$$\frac{\partial \nabla^2 \Psi}{\partial t} + \alpha J(\Psi, \nabla^2 \Psi) + \frac{\partial \Psi}{\partial x} = w_E - \gamma \nabla^2 \Psi - \mathcal{D}, \quad (\text{A1})$$

where $J(\dots, \dots)$ is the Jacobian operator, w_E is the nondimensional Ekman pumping velocity at the upper boundary, $\alpha = U/\beta d^2$, $\gamma = r/\beta d$, r is the coefficient of bottom friction, and \mathcal{D} is additional horizontal dissipation. Equation (A1) was solved numerically using the fourth-order accurate Harvard quasi-geostrophic finite-element model originally developed by Haidvogel et al. (1980) and Miller et al. (1981). Additional horizontal dissipation \mathcal{D} was included in the form of an eighth-order Shapiro filter on vorticity $\Pi = \nabla^2 \Psi$ (Shapiro 1970). The model was configured in the same way as the model used by Marshall (1984) using a flat bottomed, closed, rectangular domain given by $0 \leq x \leq 1$, $-1 \leq y \leq 1$ centered at 29.33°N and forced with a surface Ekman pumping velocity given by $w_E = w_0 \sin(\pi y)$. At the solid boundaries $\Psi = 0$, and as in Marshall (1984) the vorticity equation is solved on the boundaries. Scaling parameters identical to those used by Marshall (1984) were also chosen, namely, $U = \pi/100 \text{ m s}^{-1}$, which is the velocity scale for the Sverdrup interior flow assuming a sinusoidal variation of wind stress with latitude, where $d = 10^6 \text{ m}$, $H = 500 \text{ m}$, and $\beta = 2 \times 10^{-11} \text{ m}^{-1} \text{ s}^{-1}$, which yields $\alpha = 1.57 \times 10^{-3}$.

Two versions of the model were used in the calculations presented here and will be referred to as high resolution and low resolution. In the high-resolution model, (A1) was solved on a 55×109 grid corresponding to a horizontal resolution of 18.5 km. In this case r was chosen to be 14.47 day^{-1} , which yields $\gamma = 0.04$. The corresponding scales for the inertial boundary layer $\delta_I = \alpha^{1/2} d$ and viscous boundary layer $\delta_S = \gamma d$ are both 40 km, and resolved by the model. In the low-resolution model, (A1) was solved on a 17×33 grid, corresponding to a horizontal resolution of 62.5 km. In this case δ_I and δ_S are poorly resolved, but the Shapiro filter renders the model solutions well behaved by removing any spurious numerical noise. As a result, the two models behave qualitatively in the same way in our experiments. The low-resolution model is a valuable tool for some of the very computationally demanding calculations presented in section 5.

Both the high- and low-resolution models were forced with an Ekman pumping amplitude $w_0 = 1$, which corresponds to a wind stress of 0.1 Nm^{-2} and an Ekman pumping velocity of $4.31 \times 10^{-6} \text{ m s}^{-1}$ similar to that computed near the center of the North Atlantic subtropical gyre from observed wind stress estimates (Hellerman and Rosenstein 1983). In both models a double gyre circulation develops. The tangent linear model and adjoint models that solve the linearized forms of (A1) are described in detail by Moore (1991), Farrell and Moore (1992), and Moore and Farrell (1993).

APPENDIX B

8. The Iterative Computation of Eigenmodes, Singular Vectors, Stochastic Optimals, and Pseudospectra

All of the eigenvector calculations presented in this paper were performed using iterative techniques based on the ARPACK library of Lehoucq et al. (1997). The ARPACK routines ssaupd and snaupd compute selected eigenvalues and eigenvectors of large symmetric or nonsymmetric matrices respectively. All that the user need provide is a routine that computes the matrix-vector product, thus the elements of the matrix are not explicitly required. The routine ssaupd uses a Lanczos algorithm while in snaupd the method of Arnoldi is utilized (Golub and van Loan 1989). These are iterative algorithms in which a selected number of eigenvectors and eigenvalues are computed, their accuracy being refined with each iteration. If \mathbf{R} and \mathbf{R}^T denote the propagator of the tangent linear and adjoint tangent linear models respectively, ssaupd and snaupd can be used to compute the eigenvectors of interest discussed in this paper.

a. The basic algorithms

1. *Eigenmodes.* The eigenmodes are defined as the eigenvectors of the tangent linear propagator \mathbf{R} . Thus a forward integration of the tangent linear form of the model described in appendix A represents a matrix-vector product, which when combined with snaupd, can be used to compute the eigenmodes. The adjoint eigenmodes of \mathbf{R}^T can be computed from backward integrations of the adjoint model [cf. Eq. (7)].
2. *Singular vectors.* The singular vectors are the eigenvectors of $\mathbf{R}^T \mathbf{X} \mathbf{R}$. A matrix-vector product can be computed as a forward integration of the tangent linear model (5) followed by a multiplication by \mathbf{X} , then by a backward integration of the resulting vector by the adjoint model (7). In conjunction with ssaupd this yields the singular vectors.

3. *Stochastic optimals.* From [section 3c](#), the stochastic optimals are the eigenvectors of $\mathbf{Z} = \Delta t^2 \sum_{j=0}^{n-1} \sum_{m=0}^{n-1} D_{m,j}$ $\mathbf{R}^T_{j+1,n-1} \mathbf{X} \mathbf{R}_{m+1,n-1}$ where $D_{m,j}$ describes the temporal correlation of the stochastic forcing. By combining the algorithm of [\(2\)](#) with the trapezoidal rule the stochastic optimals can be computed using `ssaupd`.
4. *Pseudospectra.* For any complex forcing frequency ω the pseudospectra are defined as contours of $\|\mathcal{R}(\omega)\| = \|(\omega \mathbf{I} - \mathbf{A})^{-1}\|$ where \mathbf{A} is the tangent linear operator. If the 2-norm is used, then $\|\mathcal{R}(\omega)\|$ is simply given by the smallest singular value of $(\omega \mathbf{I} - \mathbf{A})$. Thus a modification of [\(2\)](#) applied to \mathbf{A} instead of \mathbf{R} can be used to compute the pseudospectra in conjunction with `enaupd`, which is the complex version of `ssaupd`.

b. Computational considerations

All of the calculations outlined above are computationally demanding and require the repeated iteration of either the tangent linear model, the adjoint model, or a combination of both. The tangent linear and adjoint models require approximately twice the CPU time of the nonlinear model for the same simulated time interval. Thus for the singular vector computations described in [\(2\)](#) a single iteration of the tangent linear and adjoint models requires approximately four times the CPU time of the nonlinear model. The computational overhead associated with the ARPACK routines is relatively small. The number of iterations required to compute N singular vectors varies considerably and is anywhere from $2N$ – $10N$. The eigenmode calculations described in [\(1\)](#) are typically much more computationally intensive than the singular vector calculations due to the non-symmetric nature of the problem, so the ratio of the number of iterations required to the number of eigenmodes requested is typically much higher, unless the entire spectrum of eigenmodes is computed.

The stochastic optimals were computed by evaluating the time integrals implicit in [\(12\)](#) using the trapezoidal rule. Care must be exercised to ensure that the resulting eigenvectors are insensitive to the number of trapezoidal intervals chosen. In our case this was determined by trial and error. The computational cost of the stochastic optimal calculations in [\(3\)](#) is much higher than for the singular vectors because the tangent linear and adjoint models must be integrated over each trapezoidal interval. If one time integral in [\(12\)](#) is divided into I intervals and the other integral into J intervals, then the total cost of one iteration of [\(12\)](#) is equivalent to $I(J + 1)/2$ iterations of the singular vector calculation in [\(2\)](#). Considerable computational savings are afforded by assuming that the stochastic forcing is white in time in which case one integral in [\(12\)](#) disappears.

For the pseudospectra calculations of [\(4\)](#), the smallest singular vectors of the inverse resolvent are computed. For other than the L2-norm, this is a computationally demanding calculation because of the repeated solution of the system of linear equations associated with the factorization matrix \mathbf{M} , where $\mathbf{X} = \mathbf{M} \mathbf{M}^T$.

As a guide to the computational cost of these calculations, a single 1 day iteration of the high resolution tangent linear and adjoint models as described in [\(2\)](#) requires approximately 2 s of CPU time on a Compaq 600 MHz Alphastation. The singular vector calculation shown in [Fig. 1b](#) was computed along with five other members of the spectrum and required 18 min of CPU time to perform 36 iterations. The Lyapunov exponent calculations of [section 5](#) require optimal growth times of several thousand days. A single 5000-day singular vector calculation using the high-resolution model requires ~ 4 days of CPU time. [Figure 12](#) and [Table 1](#) indicate that many similar calculations are required to reliably estimate κ_1 , thus these computations are computationally prohibitive for the high resolution model given the computer facilities available to us at present. The low-resolution model was therefore used instead.

The primary limiting factor for many of the calculations described here is memory and CPU time. If resources are available, there appears to be no limit on the size of the problems that can be tackled using ARPACK. Many of the calculations described here have been performed using large ocean general circulation models, and singular vector calculations are performed routinely at some operational centers using numerical weather prediction models.

Tables

TABLE 1. Estimates of the Lyapunov exponent κ_1 of the tangent linear model linearized about the time-evolving circulation depicted in Figs. 10 and 11 using different 5000-day time intervals. The uncertainty in κ_1 for each period is also indicated. The uncertainty estimate is computed by minimizing the chi-square statistic assuming that all v are weighted equally. The std dev of the v about the resulting straight line is then used to compute the uncertainty estimates of κ_1 using the standard formulas (see Press et al. 1986, their section 14.1)

Time interval (days)	Lyapunov exponent κ_1 (day) ⁻¹
10 000–15 000	$1.56 \times 10^{-2} \pm 5.7 \times 10^{-4}$
15 000–20 000	$1.46 \times 10^{-2} \pm 5.6 \times 10^{-4}$
20 000–25 000	$1.06 \times 10^{-2} \pm 3.7 \times 10^{-4}$
30 000–35 000	$1.26 \times 10^{-2} \pm 6.5 \times 10^{-4}$

[Click on thumbnail for full-sized image.](#)

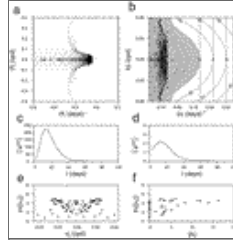
Figures





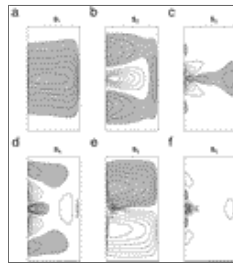
Click on thumbnail for full-sized image.

FIG. 1. (a) The wind-forced streamfunction of the ocean circulation described by the high-resolution, nonlinear, quasigeostrophic potential vorticity equation when $w_0 = 1$. The arrows indicate the sense of the circulation. (b) The vorticity field of the fastest growing singular vector of the high-resolution tangent linear model linearized about the circulation in (a). The singular vector shown maximizes the growth of perturbation enstrophy over a 14-day time interval. The factor μ_Q by which perturbation enstrophy grows over 14 days is indicated. (c) As (b), but also the streamfunction of the singular vector that maximizes the growth of perturbation energy over a 14-day time interval. The perturbation energy growth factor μ_E is indicated. Shaded and unshaded regions are of opposite sign. The contour interval in (a) is 0.1, while in (b) and (c) it is arbitrary



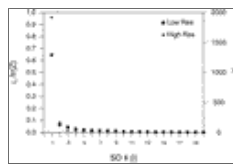
Click on thumbnail for full-sized image.

FIG. 2. (a) A general view of the eigenmode spectrum of the high-resolution tangent linear model linearized about the double gyre circulation in Fig. 1a. (b) Contour plot of $|\mathcal{R}(\omega)|$ in the vicinity of the origin of the complex frequency plane $\omega = \omega_r + i\omega_i$ for the double gyre circulation of the high-resolution model. Contour values $c = 20, 30, 50, 100, 250, 500,$ and 1000 are shown in each case, and regions where $c \geq 100$ are shaded. The dots and triangles indicate the eigenvalues of (5), and the asterisks and corresponding dashed lines indicate $\sup_{\omega \in \Lambda_c} \text{Re}(\omega)$ for selected contour values $c = \epsilon^{-1}$. The triangles also represent the eigenvalues of the eigenmodes that define the subset Λ_c (see main text for definition): (c) $\ln|v_k|$ vs σ_i for the Q -norm, (d) $\ln|v_k|$ vs t for the E -norm, (e) $\ln|v_k|$ vs σ_i for the subset of eigenmodes Λ_c of the double-gyre circulation [i.e., those eigenmodes that determine the structure of $|\mathcal{R}(\omega)|$ in (b)], (f) $\ln|v_k|$ vs $|a_k|$ where a_k is the amplitude of the projection of the singular vector in Fig. 1b on the subset of eigenmodes Λ_c of the double gyre circulation. In (e) and (f) asterisks indicate those eigenmodes for which $|a_k| \geq 8$



Click on thumbnail for full-sized image.

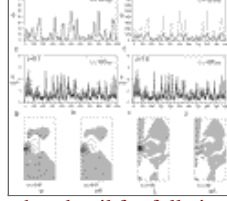
FIG. 3. The patterns of Ekman pumping velocity associated with the first six members of the stochastic optimal spectrum of the stochastically forced high-resolution tangent linear model linearized about the steady circulation of Fig. 1a. It is assumed that the stochastic forcing is white in time and a time interval of 300 days is used to compute \mathbf{Z} in (12). The perturbation enstrophy norm is used as a measure of stochastically induced variance. Shaded and unshaded regions are of opposite sign, and the contour interval is arbitrary



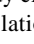
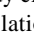

Click on thumbnail for full-sized image.

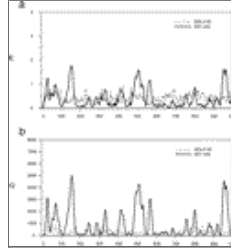
FIG. 4. The eigenvalues s_j of the first 20 stochastic optimals (SO) of both the high- and low-resolution tangent linear models linearized about the appropriate double-gyre circulation. In the case of the low-resolution model $s_j/\text{tr}(\mathbf{Z})$ is plotted and represents the fraction of stochastically induced variance in Q that would be explained by each stochastic optimal assuming that each contributes equally to the Q that is input by the stochastic forcing






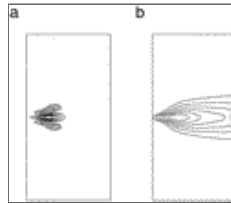
Click on thumbnail for full-sized image.

FIG. 5. (a)–(f) Time series of E , Q , and P from the stochastically forced high-resolution tangent linear model (dashed curves) linearized about the steady circulation of Fig. 1a , and ΔE , ΔQ , and ΔP from the stochastically forced nonlinear model (solid curves). The steady circulation of Fig. 1a  was generated with an Ekman pumping amplitude $w_0 = 1$. The rms stochastic forcing amplitude is ρw_0 where the values of ρ used are indicated. With $\rho = 0$ the nonlinear model yields the steady circulation of Fig. 1a . Snapshots of perturbation streamfunction and perturbation vorticity from each model on day 330 for the case $\rho = 1.0$ are shown in (g)–(j), respectively. In order to show more clearly the details, the vorticity fields are plotted only within the region enclosed by the dashed line in (g). Shaded and unshaded regions are of opposite sign, and the contour intervals (c.i.) used are indicated




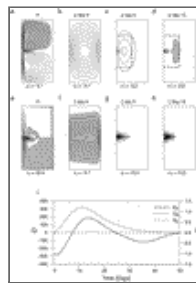
Click on thumbnail for full-sized image.

FIG. 6. Time series of (a) E and (b) Q from the stochastically forced, high-resolution, tangent linear model linearized about the steady circulation of Fig. 1a . The stochastic forcing is composed of either S_1 only (solid curve) or S_i for $i = 2, \dots, 20$ (dashed curve)



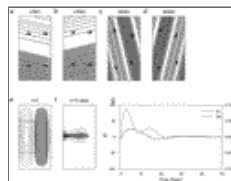
Click on thumbnail for full-sized image.

FIG. 7. The vorticity structure of (a) the least-damped eigenmode, and (b) the least-damped adjoint eigenmode, for the high-resolution tangent linear model linearized about the double-gyre circulation of Fig. 1a 



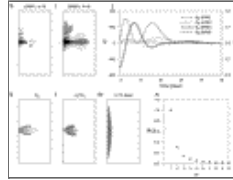
Click on thumbnail for full-sized image.

FIG. 8. The time evolution of a perturbation resembling the first stochastic optimal of the tangent linear model linearized about the steady basic state shown in (a) and (e). (b)–(d) The perturbation streamfunction ψ on selected days, and (f)–(h) the perturbation vorticity ζ . In order to show the detail, note that in (g) and (h) the vorticity is plotted only within the region indicated by dashed lines in (c) and (d). Shaded and unshaded regions are of opposite sign, and the contour interval (c.i.) is indicated. (i) The time evolution of various terms in the perturbation energy [equation \(3\)](#) and perturbation enstrophy [equation \(4\)](#)



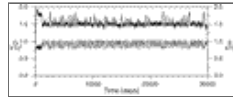
Click on thumbnail for full-sized image.

FIG. 9. Isotachs of current speed for the plane parallel Rossby waves that make up the lowest zonal wavenumber basin mode are shown as contours (a)–(d). The shaded regions indicate where $\zeta < 0$, and arrows indicate the direction of the flow. The vorticity structure of the lowest zonal wavenumber basin mode of a resting ocean (e) at $t = 0$ and (f) after 15 days of evolution on the double-gyre basic state of Fig. 1a. Note that in (f) only the vorticity within the region indicated by the dashed line in (e) is plotted. This is also the case for the fields plotted in (h), (i), (k), and (l) described below. (g) Time series of Q_R and E_R for the evolving basin mode. (h), (i) The vorticity structure of LRW1 and SRW1 after 15 days of evolution on the double-gyre circulation (the contour interval is the same in both). (j) Time series of Q_R and E_R for these cases. (k) The meridional component of the basic state vorticity gradient Π_y , and (l) the perturbation enstrophy source term $-\zeta v' \Pi_y$ for SRW1 at initial time. (m) The vorticity structure of a perturbation that initially has the structure of S_1 after it has evolved in a resting ocean for 15 days. (n) The projection $|a_m|$ vs m of S_1 on the basin modes of a resting ocean with meridional wavenumber $\pi/2$ and zonal wavenumber $m\pi$. In contour plots, shaded and unshaded regions are of opposite sign



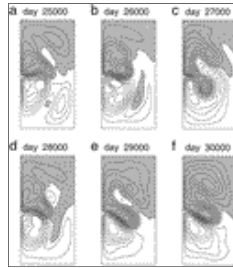
[Click on thumbnail for full-sized image.](#)

FIG. 9. (Continued)



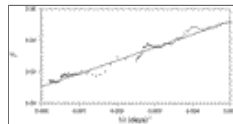
[Click on thumbnail for full-sized image.](#)

FIG. 10. Time series of basin-averaged energy (lower curve) and enstrophy (upper curve) from the unstable, low-resolution, nonlinear wind-forced model



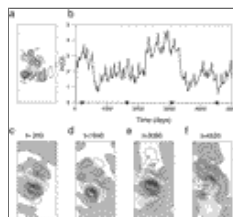
[Click on thumbnail for full-sized image.](#)

FIG. 11. Snapshots of streamfunction on selected days from the unstable, low-resolution, nonlinear, wind-forced model. Shaded and unshaded regions are of opposite sign



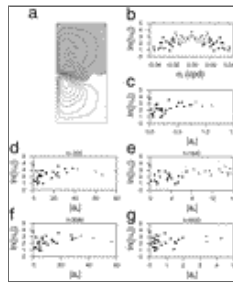
[Click on thumbnail for full-sized image.](#)

FIG. 12. Plot of v_1 vs $1/t$ computed using the low-resolution tangent linear model linearized about the time evolving solution of the nonlinear wind forced model shown in Figs. 10 and 11. Also shown is the least squares best fit straight line. The intercept of the line with the v_1 axis represents an estimate of the Lyapunov exponent κ_1



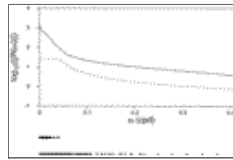
[Click on thumbnail for full-sized image.](#)

FIG. 13. (a) The initial vorticity structure of the first Lyapunov vector of the low-resolution tangent linear equation linearized about the time-evolving circulation in Figs. 10 and 11. (b) A time series of the perturbation enstrophy Q of the Lyapunov vector shown in (a). The exponential growth factor of Q given by the Lyapunov exponent κ_1 has been suppressed. (c)–(f) Perturbation streamfunction at the times indicated by stars in (b), which are approximately 1440 days apart. Shaded and unshaded



Click on thumbnail for full-sized image.

FIG. 14. (a) The time-averaged streamfunction Ψ from days 10 000–30 000 of the time-evolving circulation of [Figs. 10](#) and [11](#). Shaded and unshaded regions are of opposite sign, and the contour interval is 0.3. (b) $\ln|v_k|$ vs σ_i for the subset of eigenmodes Λ_c of \mathbf{A} evaluated using Ψ , and (c) $\ln|v_k|$ vs $|a_k|$ for the perturbation shown in [Fig. 13a](#): (d)–(g) $\ln|v_k|$ vs $|a_k|$ for each snapshot of the Lyapunov vector shown in [Figs. 13c–f](#): (c)–(g) Asterisks indicate the eigenmodes for which $|a_k| > \text{one half the maximum value}$, and (b) all the eigenmodes that satisfy this criteria at all the times shown are so indicated



Click on thumbnail for full-sized image.

FIG. 15. The solid curve shows $\log_{10}|\mathcal{R}(\omega)|$ vs ω for purely imaginary forcing ($\omega_r = 0$) for the double gyre circulation of [Fig. 1a](#). The dashed curve shows $1/\text{dist}(\omega, \Lambda)$ for the basin modes of a resting ocean. The imaginary components of the eigenfrequencies of the basin modes of a resting ocean are indicated by dots below the ω axis, and those of the subset of eigenmodes Λ_c of the double-gyre circulation are shown as asterisks

Corresponding author address: Dr. Andrew M. Moore, Program in Atmospheric and Oceanic Sciences, CIRES, University of Colorado, Campus Box 311, Boulder, CO 80309-0311. E-mail: andy@australis.colorado.edu

¹ The term “basin mode” is used here with reference to eigenmode solutions of [\(5\)](#) for a resting ocean ($\alpha = 0$) as described by [Pedlosky \(1979\)](#), his section 3.25.

² This was demonstrated in an earlier version of this paper in which only the low-resolution model was used. At the suggestion of one of the reviewers, the high-resolution model was introduced to verify our earlier findings.

top ▲



© 2008 American Meteorological Society [Privacy Policy and Disclaimer](#)
 Headquarters: 45 Beacon Street Boston, MA 02108-3693
 DC Office: 1120 G Street, NW, Suite 800 Washington DC, 20005-3826
amsinfo@ametsoc.org Phone: 617-227-2425 Fax: 617-742-8718
 Allen Press, Inc. assists in the online publication of AMS journals.